

THESIS FOR THE DEGREE OF LICENTIATE OF ENGINEERING

# Correlating structure of (arabino)xylans and their derivatives to dispersibility and film properties

Ratchawit Janewithayapun

Department of Chemistry and Chemical Engineering  
CHALMERS UNIVERSITY OF TECHNOLOGY

Göteborg, Sweden 2023

Correlating structure of (arabino)xylans and their derivatives to dispersibility and film properties  
RATCHAWIT JANEWITHAYAPUN

©RATCHAWIT JANEWITHAYAPUN, 2023

Licentiatuppsatser vid institutionen för kemi och kemiteknik  
Chalmers tekniska högskola  
Nr 2023:16

Department of Chemistry and Chemical Engineering  
Chalmers University of Technology  
SE-412 96 Göteborg  
Sweden  
Telephone: +46 (0)31-772 1000

Cover:  
Polarized light microscopy image of a modified arabinoxylan film

Printed by Chalmers Reproservice  
Göteborg, Sweden 2023

Correlating structure of (arabino)xylans and their derivatives to dispersibility and film properties

Thesis for the degree of Licentiate of Engineering

RATCHAWIT JANEWITHAYAPUN

Department of Chemistry and Chemical Engineering

Chalmers University of Technology

## ABSTRACT

Wood glucuronoxylans and wheat bran arabinoxylan represent significant sources of underutilized natural polymers. In this work, I aim to address a key challenge to their effective valorization, which is their complex chemical-structure-property relationship. I investigated how the composition of hardwood xylans affects their dispersibility in two common solvents: water and DMSO, and how this relates to the nanoscale conformations of individual xylan chains using small-angle neutron scattering. We also investigated whether introducing flexible hinges to the stiff polysaccharide chains through periodate oxidation and borohydride reduction would alter their dispersibility and conformations in these solvents. The results showed that the dispersibility of the xylans is linked to their solvent interactions, and consequently, their conformation in water or DMSO. The oxidation and reduction modification did indeed change the solvent interactions of the xylans but only led to slight improvements in dispersibility in water and, in some cases, worsened dispersibility in DMSO.

For arabinoxylan (AX), we showed that the chemical composition of AX is a large factor in controlling the mechanical properties of modified thermoplastic films. We obtained compression moldable films from AX with low and high branching ratios. The low-branched modified AX films showed more brittle and stiff behavior, whereas the higher-branched modified AX films were softer, and could be stretched up to 140 % strain. We linked the properties to their relaxation mechanisms in dynamic mechanical testing (DMA) and the nano-structures observed via X-ray scattering. The observed nano-structures involved phase separation into nano-domains, we further showed that the sizes and mobility of nano-domains were dependent on the AX structure and composition. Therefore, by selecting specific chemical compositions of AX, materials with tuneable stiffness and ductility can be designed.

**Keywords:** Thermoplasticity, hemicellulose, etherification, mechanical properties, solubility



# LIST OF PUBLICATIONS

This thesis is based on the following appended manuscripts:

Manuscript I:

**Do wood xylans only exist as aggregates in solutions?**

Chonnipa Palasingh, Ratchawit Janewithayapun, Leide P. Cavalcanti, Felix Abik, Kirsi S. Mikkonen, Fabrice Cousin, Anna Ström, Tiina Nypelö

*Manuscript*

Manuscript II:

**Nanostructures of etherified arabinoxylans and the effect of arabinose content on materials properties**

Ratchawit Janewithayapun, Mikael S. Hedenqvist, Fabrice Cousin, Alexander Idström, Lars Evenäs, Patricia Lopez Sanchez, Gunnar Westman, Anette Larsson, Anna Ström

*Manuscript*

# MY CONTRIBUTION

Manuscript I:

I performed the neutron scattering experiments (SANS) in collaboration with my co-authors, and analyzed the SANS data. I interpreted the results and co-wrote the first draft of the manuscript, which is being finalized together with my co-authors.

Manuscript II:

I planned and performed the sample extraction, modification and characterization, with exception of the diffusion NMR. I interpreted the results and wrote the first draft of the manuscript, which is being finalized together with my co-authors.



*To my family,  
whom I wish a cold and cozy winter in Thailand*





# NOTATION

ATR-FTIR	Attenuated total reflectance - Fourier transform infrared spectroscopy
AX	Arabinoxylan
BGE	Butyl glycidyl ether
BGE-diol AX	BGE grafted dialcohol arabinoxylan
DalX	Dialcohol xylan
Diol AX	Dialcohol arabinoxylan
DSC	Differential scanning calorimetry
DMA	Dynamic mechanical analysis
HPAEC	High performance anion exchange chromatography
NMR	Nuclear magnetic resonance spectroscopy
SANS	Small-angle neutron scattering
SAXS	Small-angle X-ray scattering
$T_g$	Glass transition temperature
$T_m$	Melting temperature
TGA	Thermogravimetric analysis
WAXS	Wide-angle X-ray scattering



# CONTENTS

<b>Abstract</b>	<b>iii</b>
<b>List of Publications</b>	<b>v</b>
<b>Notation</b>	<b>ix</b>
<b>Contents</b>	<b>xi</b>
<b>1 Introduction</b>	<b>1</b>
<b>2 Background</b>	<b>5</b>
2.1 Xylans from different sources . . . . .	5
2.1.1 Effect of chemical composition on solution properties . . . .	6
2.2 Periodate oxidation and reduction with sodium borohydride of polysaccharides . . . . .	7
2.3 Thermoplasticity of polysaccharides . . . . .	8
2.4 X-ray and neutron scattering . . . . .	9
2.4.1 Structures observed in wide-angle scattering . . . . .	10
2.4.2 Structures observed in small-angle scattering . . . . .	11
<b>3 Methodology</b>	<b>15</b>
3.1 Materials- Manuscript I . . . . .	15
3.1.1 Preparation of dialcohol xylan . . . . .	15
3.1.2 Preparation of xylan dispersions for SANS . . . . .	16
3.2 Materials - Manuscript II . . . . .	16
3.2.1 Alkali extraction of wheat bran AX . . . . .	16
3.2.2 Chemical modification of AX . . . . .	17
3.2.3 Film fabrication . . . . .	18
3.3 Chemical characterization . . . . .	18
3.3.1 UV-Vis spectroscopy . . . . .	18
3.3.2 HPAEC monosaccharide composition . . . . .	19
3.3.3 Attenuated total reflectance FTIR (ATR-FTIR) . . . . .	19
3.3.4 NMR . . . . .	20
3.3.5 DMA . . . . .	21
3.4 Thermomechanical characterization . . . . .	22
3.4.1 DSC . . . . .	22
3.4.2 TGA . . . . .	22

3.4.3	Tensile testing . . . . .	23
3.5	X-ray and neutron scattering . . . . .	23
3.5.1	SANS . . . . .	23
3.5.2	X-ray scattering . . . . .	23
<b>4</b>	<b>Results and Discussion</b>	<b>25</b>
4.1	Neutron scattering studies of wood xylan and dialcohol xylan dispersions . . . . .	25
4.1.1	Xylan dispersibility in water . . . . .	25
4.1.2	Xylan dispersibility in DMSO . . . . .	28
4.1.3	Dialcohol xyans in water and in DMSO . . . . .	29
4.1.4	A summary of the first section . . . . .	32
4.2	Nanostructure and thermomechanical properties of modified AX films	34
4.2.1	Chemical composition of extracted AX from wheat bran . .	34
4.2.2	Results of periodate oxidation and sodium borohydride reduction . . . . .	34
4.2.3	Results of BGE substitution . . . . .	35
4.2.4	Diffusion NMR of BGE-diol AX . . . . .	36
4.2.5	Compression molded films of BGE-diol AX . . . . .	36
4.2.6	Characterization of BGE-diol AX structures by X-ray scattering . . . . .	38
4.2.7	Thermal properties . . . . .	40
4.2.8	A summary of the second section . . . . .	43
<b>5</b>	<b>Conclusions and Future Work</b>	<b>45</b>
	<b>Acknowledgements</b>	<b>47</b>
	<b>References</b>	<b>49</b>

# 1 Introduction

Lignocellulosic materials are being developed as possible replacements for fossil fuel based materials in several application areas. The three major components of lignocellulose are cellulose, hemicellulose and lignin. Cellulose is generally regarded as the most abundant natural polymer [1], and a similarly large research effort has been directed towards its development. The utilization of wood and cereal hemicelluloses however, are not as developed.

Hemicellulose is generally defined as non-cellulosic polysaccharides that can be extracted with alkali from the depectinated cell wall [2, 3]. Another definition refers to hemicelluloses as non-cellulosic polysaccharides in plant cell walls composed of  $\beta$ -(1 $\rightarrow$ 4)-linked backbones [4]. In this thesis, the terms hemicellulose and polysaccharide are used interchangeably when referring to xylan and arabinoxylan.

Xylan based polysaccharides are the major hemicellulose component of plant cell walls - accounting for 25 - 35% of the dry weight (% w/w) in hardwoods and 5 - 10 % w/w in softwoods [5–7]. Within the EU states, Sweden holds the largest area of forested and wooded land (in 2020) [8] and is the world’s 5th largest exporter of pulp, paper and sawn timber. Around 70 million m<sup>3</sup> of wood is used as raw material in Sweden per year - sourcing the production of 12 million tonnes for pulp and 9 million tonnes of paper [8, 9]. Xylans therefore, represent a large source of underutilized natural polymers that can be obtained through the byproducts of the already active forest economy.

Arabinoxylans (AX) are a subtype of xylan-based polysaccharides, constituting the main hemicellulose component in cereals such as wheat, rye, barley and rice [10]. Wheat is a particularly essential cereal grown in the region with Sweden harvesting over 5 million tonnes of wheat grain in 2022 [11], of which around 15 % w/w (or 0.75 million tonnes) is wheat bran. Most of the AX content in wheat grain is concentrated in the outer bran, while the endosperm contains mostly starch. AX makes up only 1-2 % w/w of the endosperm compared to 10 - 30 % w/w in wheat bran [12–15]. As the bran is typically removed prior to consumption, wheat bran can be obtained as a side-stream of the agricultural industry, thus making AX another good potential source of natural polymers.

The low utilization rate of hemicelluloses comes from economic challenges - high costs of extraction and processing, and from intrinsic material challenges associated with hemicelluloses themselves. Some of the material-intrinsic barriers

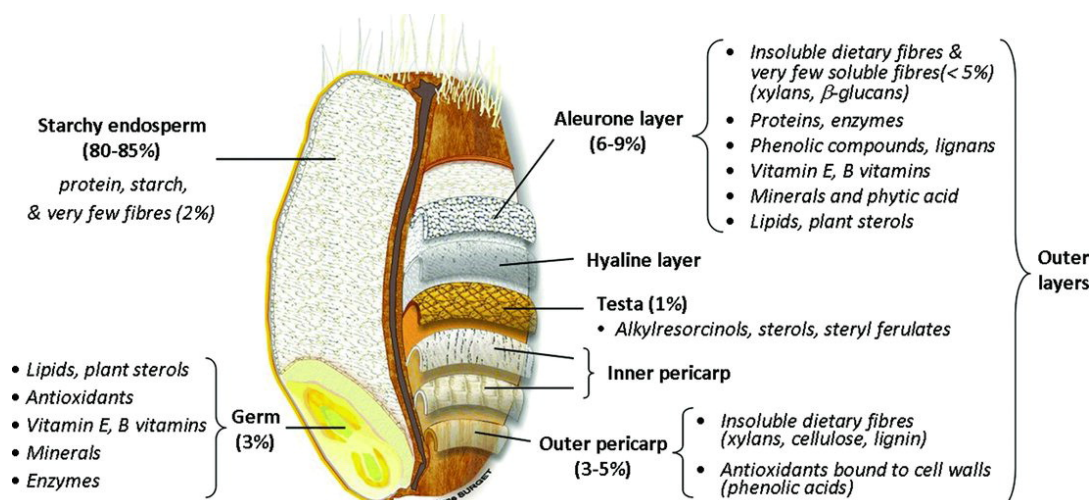


**Figure 1.1:** Structure of the wheat grain. Reproduced with permission from Brouns et al., Taylor & Francis 2012

are for example, moisture sensitivity, brittleness when made into films, chemical structure diversity and unprocessability by melt processing. The objective of this thesis is to contribute to a better understanding and solution for the two last challenges.

The chemical composition of xylan and AX vary, not only between cereals, hardwoods and softwoods, but also between species within the same category. Variations and distributions can even be found within the same plant species - depending on the growth environment and extraction process. Their solution properties are strongly affected by their chemical compositions, more so than their molecular weights. Different chemical compositions within xylan and AX can result in the formation of nano to micro-sized particles, gel networks or even solubilized chains [17–22]. The former may be useful for preparing coatings for cellulosic surfaces or for pharmaceutical nanoparticles [18, 23]. However, well dispersed chains are preferred for functionalization reactions and analytical chemistry [10, 24].

The first section of the thesis investigates the relationship between chemical composition and molecular conformation of hardwood xylans and wheat bran AX and how the solvent dispersibility is affected. The hypothesis is that by increasing the flexibility of the xylose backbone, the dispersibility of xylans can be improved irregardless of their chemical compositions. This could be expected through a change in polysaccharide-solvent interaction and/or entropy gain due to increased conformation possibilities. This will be studied by investigating xylan conformations using small angle X-ray and neutron scattering methods.

Similar to other plant-based polymers and macromolecules, xylan and AX cannot be melt-processed in its native state [25, 26]. In order to achieve melt-processability, previous work has shown that a sequence of

oxidation-reduction-etherification reactions resulted in a modified AX film that could be compression molded, and stretched above 100 % strain [25]. Questions remain however, on the exact mechanisms behind the modification, and the correlation of changes in molecular and nanostructure to the achieved thermoplasticity.

The hypothesis is that the starting molecular structure of AX has an affect on the success of the modification. This could be indirectly through different reactivity and solubility during the reaction. Or directly, where the structural features such as crystallinity and branching density directly control the property of the final product. The thermomechanical properties are compared and the structures of the melt compressed films were studied using small and wide angle X-ray scattering.





## 2 Background

### 2.1 Xylans from different sources

The thesis focuses on the study of xylans from two different sources, hardwood and wheatbran.

Xylans are linear polysaccharides with a backbone of  $\beta$ -(1 $\rightarrow$ 4)-D-xylopyranosyl units [5]. The xylans investigated in manuscript II were extracted from hardwood trees, where they are mostly present as glucuronoxylans. These contain 4-O-methyl-D-glucuronic acid (MeGlcA) and glucuronic acid (GlcA) side groups linked to the xylose residues through an  $\alpha$ -(1 $\rightarrow$ 2) linkage. The (Me)GlcA: xylose ratio can vary between 0.06 and 0.25 depending on the extraction process and material source [10]. The xylose residues can also be partially acetylated, with acetylation degrees as high as 0.6, although some acetyl groups are lost during alkaline extraction and isolated xylans generally retain an acetylation degree between 0.03 and 0.13 [5, 10]. Figures 2.1 (a) and (b) show the main linkages and substitutions present in hardwood xylan. Conventionally, the term xylan is used for all xylose-based hemicelluloses in hardwood and softwood - the same nomenclature is followed in this thesis.

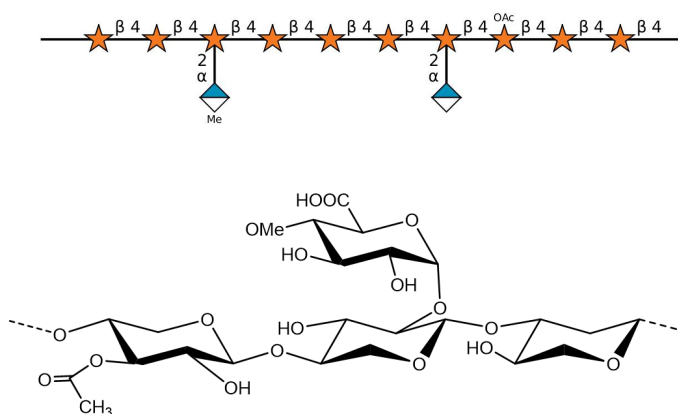


**Figure 2.1:** (a) IUPAC symbol representation of glucuronoxylan. The xylose backbone can be partially acetylated, and can be substituted with both MeGlcA and GlcA groups, (b) glucuronoxylan chemical structure showing a MeGlcA group and one acetylated xylose unit

Arabinoxylan (AX) is a xylose-based hemicellulose with partial substitution of

$\alpha$ -L-arabinofuranosyl units on O-3 and/or O-2 of xylose units resulting in a mono or disubstituted xylose unit [27]. As mentioned in the introduction, this work mainly deals with AX extracted from wheat bran where the degree of arabinose substitution is rather high - with values between 0.6 - 1.0. In comparison, substitution degrees in oat is around 0.2 and for barley husk around 0.3 [25, 28]. The composition of AX within the bran also varies strongly throughout its layers. AX from the outer pericarp region contains a higher substitution of arabinose (around 1.0) while the inner aleurone layer contains AX with substitution degree around 0.3 [27]. Other substituents such as glucuronic acids, ferulic acid and carbohydrates such as galactose may also be present [10, 27]. Ferulic acid content is however low for alkali extracted AX, owing to cleavage of the ester bond [29]. Figures 2.2 (a) and (b) show the main linkages and substitutions present in wheat bran AX.

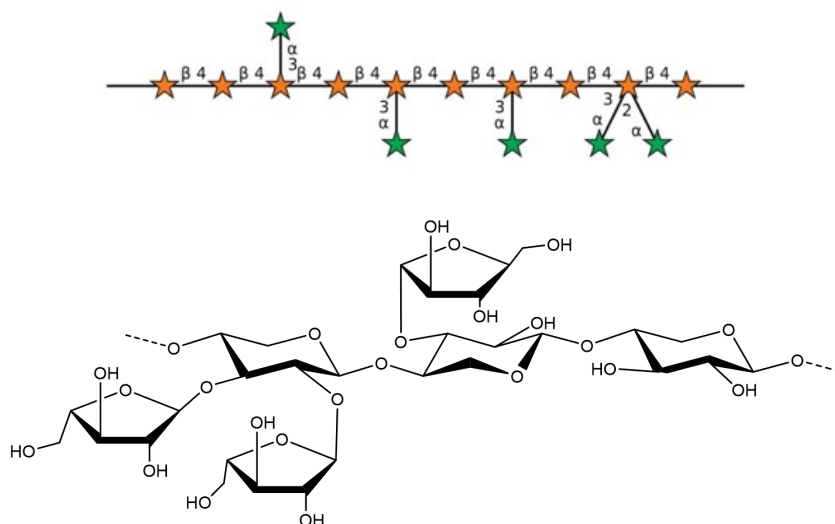


**Figure 2.2:** (a) IUPAC symbol representation of arabinoxylan. Arabinose groups are substituted onto a xylose backbone (b) Chemical structure showing arabinose substitution onto a xylose backbone

### 2.1.1 Effect of chemical composition on solution properties

For wood xylans, low substituted molecules have a strong tendency to form strong interchain interactions - resulting in nano to micrometer-sized aggregates in water [18]. Xylans with higher substitution contents are generally better dispersed in water, although usually not completely, and the improvement is affected to different degrees by the substituents present: acetyl groups, other carbohydrates, acid groups, and lignin [17]. The loss of (Me)GlcA groups was found to decrease water dispersibility [24, 30], small amounts of acetylation (10

%) improve dispersibility in water [17], while full acetylation leads instead to water indispersibility [31].

Similarly, the solubility of AX strongly depends on the amount of arabinose substituents on the xylose backbone. AX with arabinose: xylose ratios less than 0.3 are water insoluble [10]. While those with arabinose higher contents (0.3-1.2) are well dispersed or almost fully soluble in water [10, 32]. Pitkänen et al. demonstrated that it is more specifically the amount of unsubstituted xylose units on the backbone that govern the water solubility by selectively cleaving monosubstituted arabinose groups, and AX with differing substitution distributions have been discussed to have different gel-forming properties [32, 33]. The change in water solubility with arabinose content allows for different compositions to be separated using graded solvent fractionation. This method, usually by increasing ethanol concentration to precipitate AX, has been used to study AX from a variety of sources such as wheat grain, bran and rye [20, 27, 34]

For both hardwood xylans and wheat bran AX, it is understood that poor solvent dispersibility comes from the strong hydrogen bonding that occurs between sections of unsubstituted xylan units leading to aggregation [18–21]. Although some hydrophobic effects such as from lignin groups could also play a role [17, 30]

The molar mass of xylan and AX do not play a large role in determining solvent dispersibility. Saake et al., showed that xylan fractions dissolved in DMSO were similar in weight average molecular weight ( $M_w$ ) to fractions dissolved in water [17]. Schooneveld-Bergmans et al. fractionated AX using different ethanol concentrations, with most of the fractions have the same  $M_w$  (determined by SEC viscometry data) [27].

## 2.2 Periodate oxidation and reduction with sodium borohydride of polysaccharides

Periodate oxidation is a selective oxidation method using the sodium metaperiodate salt ( $\text{NaIO}_4$ ). The reaction proceeds via the formation cyclic periodate ester which decomposes to form the final product - a dialdehyde group [35–37]. The mechanism of the reaction allows it to be selective towards vicinal diols (two hydroxyl groups on adjacent carbons). This has made the periodate oxidation of great interest in the polysaccharide community as this means that the reaction will selectively cleave the C2-C3 bond in cellulose, xylans, AXs and other polysaccharides [23, 35, 38–40].

Dialdehyde groups are highly prone to forming hydrates, hemiacetals, and hemialdals in equilibrium in water [23, 35, 38]. To prevent these transient reactions, which can also lead to crosslinking between polysaccharide chains, it is common to perform a reduction with sodium borohydride ( $\text{NaBH}_4$ ) which reduces the dialdehyde groups to dialcohol groups, [23, 35]. Both the dialdehyde and

dialcohol structure for ring-opened AX is shown in Figure 2.3.

Originally, periodate oxidation has been used for analytical purposes [41]. However, interest has resurged in recent years towards utilising periodate oxidation for material development purposes [40]. The dialdehyde group formed on the polysaccharides are expected to alter their solvent interaction properties, and introduce flexible hinges to rigid stiff polysaccharide structures [23], as well as play a role in improving the ductility of the materials [40, 42]. The ring-opening has also been shown to reduce the persistence length in rigid polysaccharides such as alginates (from 15 nm to 5 nm), chitosan and celluloses [40, 43, 44]. Furthermore, dialdehyde celluloses were found to be soluble in hot water [45].

While in many cases, flexibility was seen with the dialdehyde step, such as with alginates [40, 43, 44], the dialdehyde polysaccharide can also aggregate to form compact structures [40]. The subsequent reduction to form dialcohol groups were then necessary to observe the increased flexibility of the material. This has been observed for dialdehyde celluloses to dialcohol celluloses [40], and dialdehyde xylans to dialcohol xylans [23] in water.

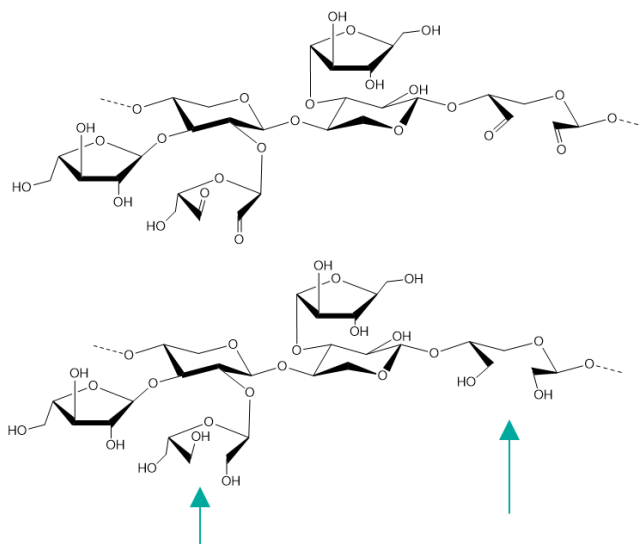


**Figure 2.3:** The chemical structure of top) dialdehyde AX, bottom) dialcohol AX. Open arabinose ring and one open xylose ring are indicated by arrows.

## 2.3 Thermoplasticity of polysaccharides

Polysaccharides in their native state are not thermoplastic - by the simplest definition, this means that they cannot be shaped through the methods with which we use to produce our plastic materials today such as compression molding, extrusion or injection molding [25, 40]. The rigid ring structures and strong intermolecular interactions between the chains reduce the mobility of the

material. This means that their relaxation temperatures are high, for amorphous polysaccharides this is related to their glass transition temperature  $T_g$ . For semi-crystalline polysaccharides, a melting temperature  $T_m$  associated with the ordered regions is also involved. For a material to be melt processable, they need to soften or flow before they start to be thermally degraded. That is,  $T_g$  (and  $T_m$ ) needs to be lower than the material's degradation temperature. Often by more than 10 °C as the measured transition temperatures are a broad distribution, and represent only the onset of softening in the material [25, 46]. The  $T_g$  of unmodified AX has been measured as 220 °C [47], while the thermal degradation of AX begins around 150 °C, with the material losing 20 % of its mass by thermogravimetric analysis (TGA) at that temperature [25].

A sequence of oxidation-reduction-etherification reactions developed had shown that it is possible to achieve modified AX materials with  $T_g$  below 130 °C while increasing degradation onset temperatures to above 250 °C [25]. Some fundamental questions remain about the process, however, one being that the process seemed to be affected by the starting material [48]. This leads to the second hypothesis stated in the introduction where I aim to investigate how the structural features of the starting material affect the thermomechanical properties of the final product.

## 2.4 X-ray and neutron scattering

In this thesis, wide-angle X-ray scattering (WAXS), small-angle X-ray scattering (SAXS), and small-angle neutron scattering (SANS) were used to characterize the hemicellulosic materials on an Ångströms to nanometer length scale. A schematic showing the length scales probed with the wavelengths of neutrons and X-rays in relation to other techniques when observing a plant cell wall is shown in Figure 2.4. In X-ray and neutron scattering, the incident probe is directed towards the sample where the probing wave is scattered by the electron shell or nuclei of atoms in the sample (for X-rays and neutrons respectively). The scattering vector  $\vec{q}$  is defined as

$$\vec{q} = \vec{k}_i - \vec{k}_f \quad (2.1)$$

where  $k_i$  and  $k_f$  are the wave vectors of the incident and scattered X-ray or neutron respectively. The techniques used are elastic, meaning that the energy of the X-rays or neutrons are not changed by interaction with the electron or nuclei and  $||\vec{k}_i|| = ||\vec{k}_f||$  [49, 50].  $\vec{q}$  is a vector in reciprocal space, corresponding to a real space distance ( $d$ ) through the relation

$$d = 2\pi/q \quad (2.2)$$

Therefore, by looking at the intensity of scattered X-ray or neutrons as a function of  $q$ , we can obtain information about the positions of atoms in the sample, and the patterns in which they are arranged.

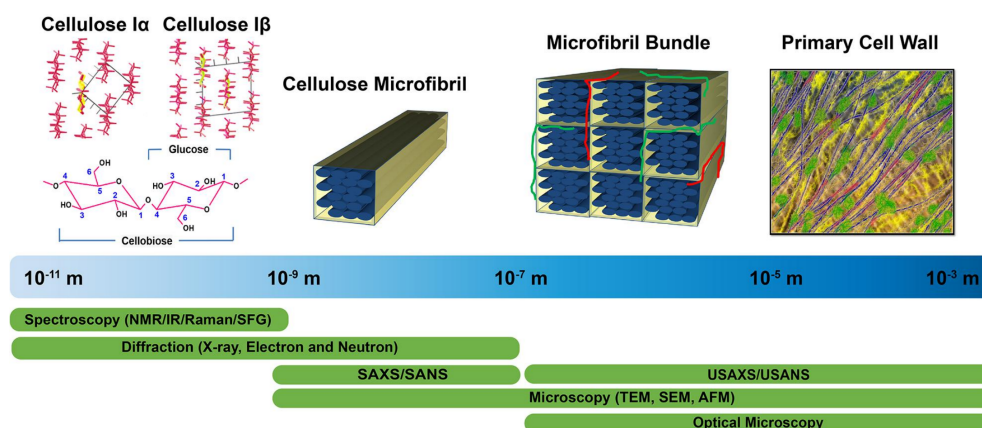


**Figure 2.4:** Different characterization methods and their length scales applied to a lignocellulosic material. Figure from Rongpipi et al. (*Frontiers in Plant Science* 2019) reproduced under the CC-BY license [51].

### 2.4.1 Structures observed in wide-angle scattering

The real space distance probed by wide-angle scattering is around 2 - 90 Å - providing information on structures such as crystalline lattices, ordered regions, and intra and intermolecular distances in polymers [46, 49, 52].

WAXS (also called X-ray diffraction) have been used to determine the unit cell of xylans and AX in the solid state [19, 53–57]. In these studies, films for fiber diffraction with higher crystallinity were prepared through solvent casting, heat treatment and stretching processes [55, 56]. Both xylan and AX were found to adopt a left-handed threefold screw helix structure stabilized by water with two chains per unit cell [53, 57]. The degree of crystallinity has been studied for AX with varying degrees of arabinose substitutions, with the lower branched specimens being closer to a linear unsubstituted xylan chain [19, 58]. Highly substituted AX is mostly amorphous [19] while AX with substitution degrees below 0.3 are semi-crystalline, with assigned degrees of crystallinity between 10 - 20 % [19, 58]. The degree of crystallinity was found to affect moisture sorption and oxygen permeability [19] and strongly change their interaction with celluloses [58]. However, the impact on the mechanical strength was found to be relatively small, with AX behaving as a brittle material regardless of the degree of crystallinity.

Other types of ordered structures can also be observed in branched polymers. An additional peak to conventional atomic distances is observed as a peak at approximately  $0.3 \text{ Å}^{-1}$  ( $3 \text{ nm}^{-1}$ ). The peak shifts to lower  $q$  values, indicating an increase in structure size with increasing side chain length [52, 59–61]. The structure was first studied in polyacrylates and polymethacrylates, and an example is taken from a study on poly( $n$ -alkyl methacrylates) (PnMMA) (Figure 2.5), with chemical structure as shown in Figure 2.5b [52, 60]. This occurs in cases where an immiscible side chain causes nanoscale separation into side chain and

backbone rich regions, a peak occurs representing the distances between backbone chains ( $d_{II}$  in Figure 2.5c). The larger 3D structure described by [60] is shown in the second illustration of Figure 2.5c. For polysaccharides, the same behavior was observed in alkyl celluloses and in chitosan [61, 62].

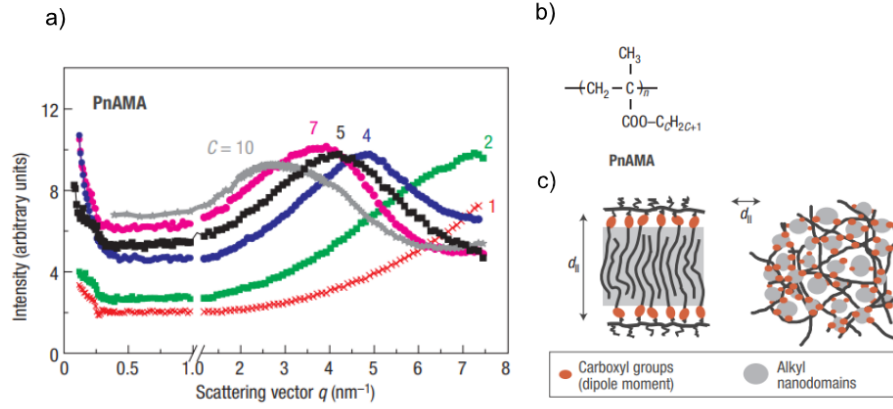


**Figure 2.5:** a) X-ray scattering data for different poly(*n*-alkyl methacrylates) (PnMMA), the number of carbon atoms in the alkyl side chain is indicated in the figure. b) chemical structure of (PnMMA). c) illustration of nanoscale phase separation in the system. Figure adapted from Beiner, M.; Huth, H. Nanophase separation and hindered glass transition in side-chain polymers. *Nature materials* **2003**, 2, 595–599 with permission from Springer Nature.

## 2.4.2 Structures observed in small-angle scattering

In this thesis, SAXS and SANS were used to investigate the behavior of xylans and AX in solution. Information on the location of the scattering particles ( $p$ ) in a solvent media ( $m$ ) can be obtained from the scattering intensity ( $I$ ) as a function of  $q$  according to

$$I(q)(\text{cm}^{-1}) = (\rho_p - \rho_m)^2 N_p V_p^2 (P(q) + N_p Q(q)) \quad (2.3)$$

where  $(\rho_p - \rho_m)$  with units (cm<sup>-2</sup>) is the difference in scattering length density (SLD) between the particle and media,  $N_p$  is the number density of particles and  $V_p$  is the volume of one particle. In practice, the volume fraction  $\phi_p$  ( $N_p V_p$ ) is known and  $V_p$  is obtained from fitting of the scattering curve [50, 63].  $P(q)$  is the form factor of the particle - the scattering contributions from scatterers belonging to the same particle.  $Q(q)$  is the structure factor - the scattering contributions from inter-particle interactions. In cases of rigid particles with centro-symmetry, such as colloids, the scattering is independent of orientation and the structure factor is written as  $S(q)$  and Equation 2.3 written instead as

$$I(q) = (\rho_p - \rho_m)^2 N_p V_p^2 P(q) S(q) \quad (2.4)$$

$S(q)$  represents the distance from the center of mass of the particles, such as in the structure factor of hard spheres [64], unfortunately, that is not the case with polysaccharides, which are not centro-symmetric. A lot of information can still be extracted from an analysis of the structure factor however. The attractive or repulsive interactions, the range of the interaction, as well as their strengths can be observed. At  $(q \rightarrow 0)$  the value of  $S(q)$  or  $Q(q)$  is related to the isothermal compressibility of the system  $\chi_T$ . At low  $q$ , an attractive system with high compressibility has values of  $S(q)$  above 1 and  $I(q)$  increases due to aggregation at low  $q$  values. For a repulsive system with low compressibility,  $S(q)$  is below 1 at low  $q$ , and  $I(q)$  decreases and oscillates with the distance of the interaction [63]. For heterogenous systems, a correlation length  $\xi$  representing the shortest distance between two monomer on separate polymer chains, a measure of the mesh size can also be extracted. [65, 66].

### Form factors of xylans and AX

Measurements of AX from different sources have been performed using both SAXS and SANS [33, 65, 67–69], while measurements on wood xylans seem to not have been reported - possibly due to the greater difficulty of obtaining samples with sufficient dispersibility. Shrestha et al. studied AX with enzymatically reduced AX content, showing an increase in aggregation with the reduction. However, the AX scattering data have only been analyzed and fitted in detail by Yu et al. [33] and recently by Petermann et al. [65]. Yu et al. reported measurements on gelling AX fractions from *P.ovata* mucilage. These are highly branched AX with distinctly different linkages compared to those found in wheat - with a significant amount of 1,3-xyl linkages. Petermann et al. performed measurements on one fraction of purified wheat flour AX with an arabinose substitution degree of 0.38, measuring the contributions of both the structure factor and the form factor in detail through a concentration series [65].

The solution conformation of AX has been described as semi-flexible chains in a good solvent (with excluded volume effects) [33, 65]. In the high  $q$  region ( $0.1 \text{ \AA}^{-1} < q < 0.5 \text{ \AA}^{-1}$ ), the scattering curve has a scaling of  $q^{-1}$ , representing scattering from an object with a mass fractal dimension of 1, indicating a rod-like shape [70]. In the intermediate  $Q$  region, probing distances of around 10 to 50 nm, ( $0.01 \text{ \AA}^{-1} < q < 0.1 \text{ \AA}^{-1}$ ), the scattering curve of AX scales with  $q^{-1.7}$ . This is the mass fractal dimension of a polymer chain in a good solvent [65, 70]. The exponent also corresponds to the Flory exponent of the polymer chain [70, 71]. Lastly, at low  $q$  values ( $q < 0.1 \text{ \AA}^{-1}$ ), we approach the theoretical region for a guinier regime [63, 65] where the size of a single chain should be observable. For AX measured by Petermann et al. the contributions from larger structures begin to dominate instead. The scattering curves measured by Petermann et al. is reproduced in Figure 2.6.



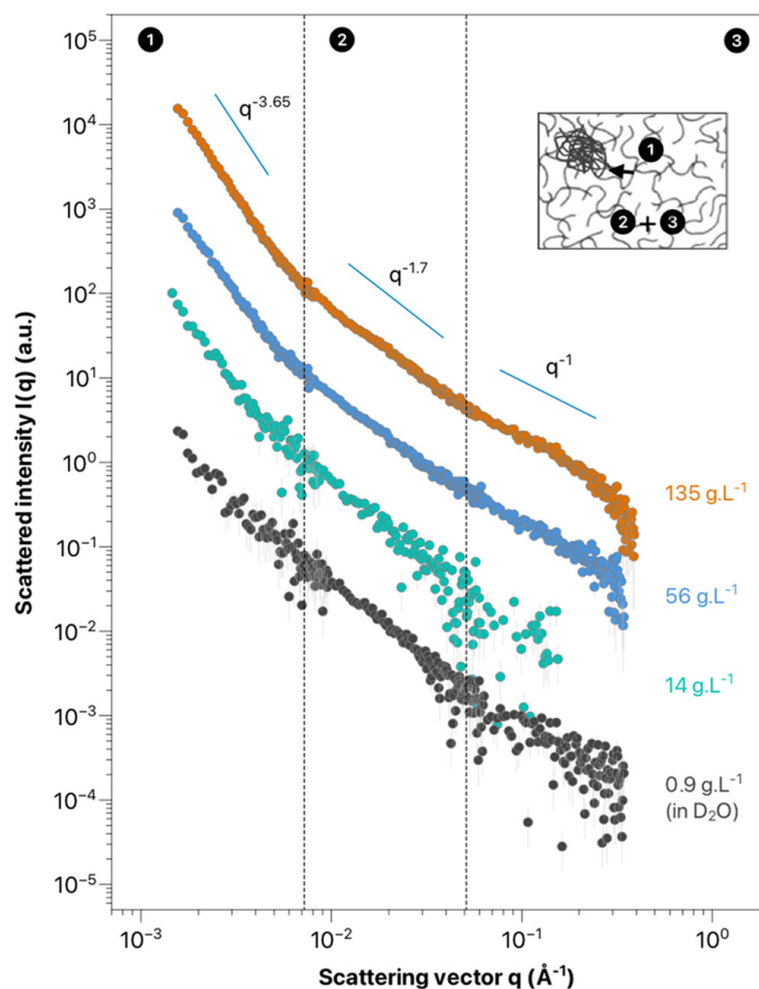


**Figure 2.6:** SANS data of wheat flour AX in  $D_2O$ , the concentrations are noted on the right, and the intensities have been shifted by the authors for ease of viewing. The low  $q$  region is denoted 1, intermediate  $q$  is 2 and the high  $q$  region is 3. The top right corner contains an illustration of the structures observed in each region. Adapted with permission from Petermann, M. et al. *Arabinoxylan in Water through SANS: Single-Chain Conformation, Chain Overlap, and Clustering*. *Biomacromolecules* **2023**, 24, 3619–3628. Copyright 2023 American Chemical Society.



## 3 Methodology

A detailed description of the modification procedure for oxidation, reduction and etherification of AX, as well as the characterization methods used are presented in this chapter. Several characterization methods were employed to probe the chemical structure of modified AX including; high performance anion exchange chromatography (HPAEC), Fourier transform infrared spectroscopy (FTIR), nuclear magnetic resonance spectroscopy (NMR) and, for oxidation monitoring, ultraviolet visible spectroscopy (UV-Vis). Characterization of thermo-mechanical properties, such as thermal relaxations and ductility, were done using dynamic mechanical analysis (DMA), differential scanning calorimetry (DSC), thermogravimetric analysis (TGA) and tensile testing. Lastly, the nanoscale structure as solid films and in solution was characterized via X-ray (SAXS/WAXS) and neutron scattering (SANS).

### 3.1 Materials- Manuscript I

Two batches of commercially available beechwood xylan and one batch of birchwood xylan were used in the study. The xylans were named in order of increasing molecular weight ( $M_w$ ) as X1, X2, and X3, respectively. X1 and X2 are beechwood xylans purchased from Megazyme Ltd. (Ireland) and Sigma Aldrich (Sweden) respectively. X3 was obtained from birchwood and was purchased from Sigma Aldrich (Sweden). The xylans were used without further purification. The compositions and properties of the xylans is shown in Table 4.1.

Sodium periodate, sodium borohydride, ethylene glycol, DMSO, D<sub>2</sub>O and DMSO-d<sub>6</sub> were acquired from Sigma Aldrich (Sweden). Pullulan standards were purchased from Postnova Analytics (Germany).

#### 3.1.1 Preparation of dialcohol xylan

Periodate oxidation and reduction of xylans were performed in X1 and X2 by Dr. Chonnipa Palasingh based on the same methods developed and used in her research group [38, 72]. Information on the degree of oxidation (DO) and  $M_w$  is shown in Table 4.2

### 3.1.2 Preparation of xylan dispersions for SANS

Xylans and dialcohol xylans were dispersed in D<sub>2</sub>O or DMSO-d<sub>6</sub>. For the DMSO-d<sub>6</sub> systems, xylans and dialcohol xylans were pre-swollen in D<sub>2</sub>O (160 µl for 1 ml total volume) overnight before dispersion in DMSO-d<sub>6</sub>. The dispersions were prepared at concentrations of 10, 20 and 30 mg/ml of xylan.

## 3.2 Materials - Manuscript II

The wheat bran was kindly provided by Lantmännen. The bran was then milled and sieved through a 1 mm mesh. Chemicals used for the extraction: hydrochloric acid, sodium chlorite (NaClO<sub>2</sub>), sodium hydroxide, sodium dithionite (Na<sub>2</sub>S<sub>2</sub>O<sub>4</sub>) were purchased from Sigma-Aldrich (Schnelldorf, Germany). Ethanol (95%) was purchased from Solveco (Rosersberg, Sweden).  $\alpha$ -amylase from *Bacillus Licheniformis* > 500 units/mg protein was purchased from Sigma-Aldrich (Schnelldorf, Germany) and  $\beta$ -glucanase (EC.2.1.73) from *Bacillus Subtilis* was purchased from Megazyme (Wicklow, Ireland). Chemicals used for the oxidation, reduction, and etherification reactions: sodium periodate (NaIO<sub>4</sub>), sodium borohydride (NaBH<sub>4</sub>), sodium phosphate monobasic (NaH<sub>2</sub>PO<sub>4</sub>), butyl glycidyl ether (BGE) were purchased from Sigma-Aldrich (Schnelldorf, Germany). The chemicals were used without further purification. Deionized (DI) water was used throughout the experiments. Regenerated cellulose dialysis membrane (Spectra/Por 3) with a molecular weight cutoff of 3.5 kDa was purchased from Spectrum Laboratories (Rancho Dominguez, CA).

### 3.2.1 Alkali extraction of wheat bran AX

AX was isolated from wheat bran on a 1 kg scale using an alkaline extraction process, described in more detail in manuscript II. Briefly, wheat bran was pretreated in acid, delignified with NaClO<sub>2</sub> and AX was extracted under alkaline conditions with Na<sub>2</sub>S<sub>2</sub>O<sub>4</sub> as a reducing agent. The hemicellulose dispersion was separated from the cellulose fraction by centrifugation. The extracted hemicellulose dispersion containing AX was concentrated to half-volume. Fractionation via sequential precipitation in increasing concentrations of ethanol (EtOH) followed (20, 40, 60 and 80% v/v). The precipitate was then recovered by centrifugation and dialyzed against DI water through a dialysis membrane with cutoff of 3.5 kDa.

The AX fractions obtained were named after their arabinose: xylose ratio as AX0.3, AX0.5, and AX0.9. Extra purification steps were performed for AX0.3 to remove  $\beta$ -glucan and obtain a purer AX material. A schematic of the process is shown in Figure 3.1.

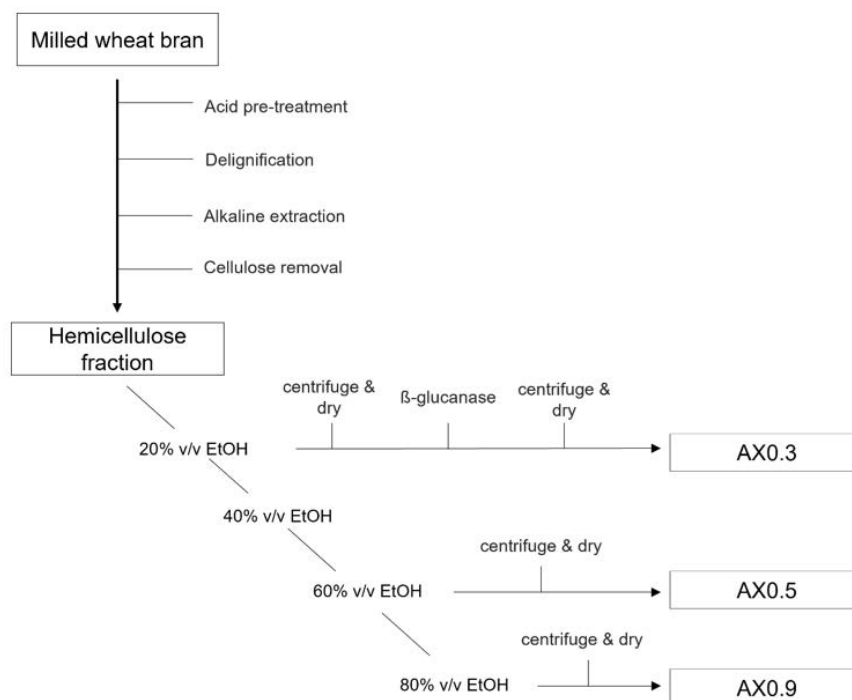


**Figure 3.1:** Fractionation of wheat bran AX through precipitation in increasing concentrations of ethanol. The fraction from 20% v/v EtOH precipitation was further purified to remove  $\beta$ -glucan which co-precipitated with the other insoluble compounds during centrifugation.

### 3.2.2 Chemical modification of AX

Chemical modification was performed to achieve an etherified ring-opened AX based on conditions used in previous works [25, 39, 48].

#### Periodate oxidation and sodium borohydride reduction of AX

To each AX fraction ((2g, 15.14 mmol AXU) was added DI water (82.5 mL) and isopropanol (5 mL). An amount of  $\text{NaIO}_4$  (0.810 g, 3.8 mmol, 0.25 equiv.) to reach a degree of oxidation (DO) of 20 % was then added. The reaction mixture was protected from light and stirred at room temperature for 17 hours.

The dialdehyde groups were reduced into dialcohol groups using  $\text{NaBH}_4$  (1 g, 26.43 mmol, 1.75 equiv.) with a sodium phosphate buffer  $\text{NaH}_2\text{PO}_4$  (0.15 g) pre-dissolved in DI water (25 mL), and added to the oxidized AX dispersion. The reduction was carried out with stirring for 4 h at room temperature. The samples were then purified through dialysis against DI water for two days with repeated changes of water. After dialysis, the samples were collected and stored at 4 °C. The oxidized and reduced AX material with dialcohol groups are designated Diol AX.

## Etherification of DiolAX

The DiolAX solution from the previous step was reduced in volume on a rotary evaporator, resulting in a concentration of ca. 4 % AX in water. NaOH (1.82 g, 45.5 mmol, 3 equiv.) was added to the 4 % AX under N<sub>2</sub> flow. Then, butyl glycidyl ether (BGE) (5.92 g, 45.5 mmol, 3 equiv.), in a 1:1 molar ratio with NaOH, was slowly added to the solution through a needle over 30 min. The mixture was stirred overnight at 45 °C. After the reaction, the solutions were neutralized with 1 M H<sub>2</sub>SO<sub>4</sub> and dialyzed against DI water for two days. The BGE modified DiolAX was recovered from dialysis by centrifugation and air dried in a convection oven at 30 °C. These samples are called BGE-Diol AX. The final chemical structure is illustrated in Figure 3.2.

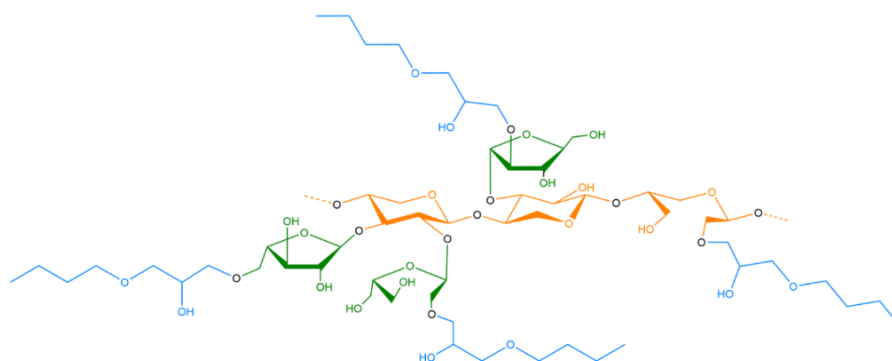


**Figure 3.2:** An illustration of the chemical structure of BGE-diol AX. Orange sections represent xylose units, green – arabinose units and blue – BGE side chains

### 3.2.3 Film fabrication

The films of BGE-diol AX materials were prepared by compression molding. The dried samples were weighed into a mold with dimensions 50 mm x 50 mm x 0.1 mm and pressed between woven Teflon sheets supported by two metal plates at 140 °C for one min without pressure to heat up and soften the samples, and then kept at 140 °C for three minutes under 50 kPa pressure. The mold was then removed, metal blocks placed over to maintain compression, and the films were allowed to cool overnight at room temperature.

## 3.3 Chemical characterization

### 3.3.1 UV-Vis spectroscopy

The progress of the oxidation reaction was followed with ultraviolet spectroscopy (UV-Vis) (Cary 60 UV-Vis, Agilent technologies, USA) by studying the

absorption band at  $\lambda = 290$  nm corresponding to the concentration of  $\text{IO}_4^-$ . A linear standard curve for the periodate solution at  $\lambda = 290$  nm was obtained using concentrations of  $\text{NaIO}_4$  between 0.1 to 5 mM. By monitoring the change in  $\text{IO}_4^-$ , an estimate of the degree of oxidation with reaction progress was obtained.

### 3.3.2 HPAEC monosaccharide composition

By hydrolyzing all of the polysaccharides present in the sample to their constituent monosaccharides, the composition of sugar monomers in the sample can be analyzed. Hydrolysis was carried out with 72 % sulfuric acid in an autoclave at 120 °C. Fucose was added to each sample as an internal standard.

A high-performance anion exchange chromatography with pulsed amperometric detection (HPAEC-PAD) using an ion chromatography system ICS 3000 (Dionex, Thermo Fisher Scientific) equipped with a CarboPac PA1 ( $4 \times 250$  mm<sup>2</sup>) analytical column separates the monosaccharides and analyzes the peaks against a known calibration mixture of pure monosaccharides. Retention time is used to identify the monosaccharide, while the area under the peak and of the fucose internal standard is used to calculate the concentration. The eluent for the system is Milli-Q water, with a 200 mM NaOH solution added post-column for the detector. An example of a HPAEC chromatogram of a sugar calibration standard sample is shown in Figure 3.3. The concentrations and type of monosaccharide analyzed can be adjusted by changing the calibration method.

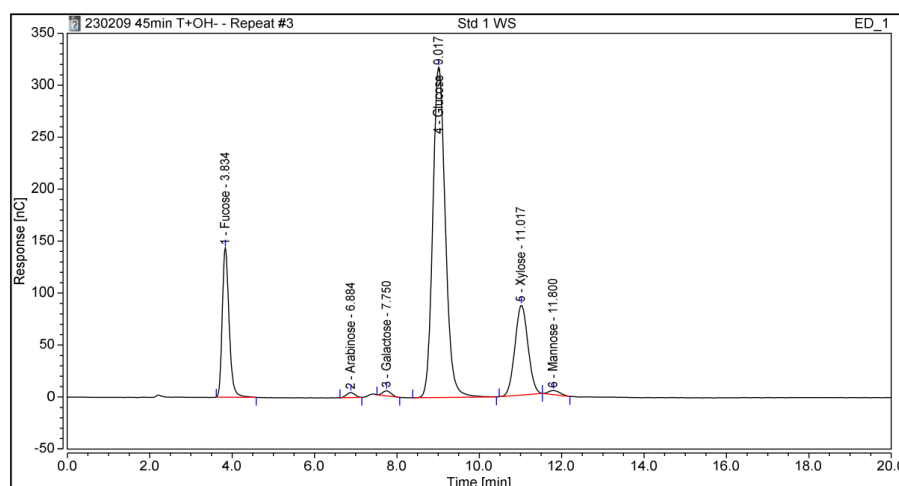


**Figure 3.3:** A chromatogram of a wood sugar calibration standard from the HPAEC method. The peaks are assigned to known values for each monosaccharide.

### 3.3.3 Attenuated total reflectance FTIR (ATR-FTIR)

Fourier transform infrared spectroscopy (FTIR) uses IR radiation with different wavelengths to probe the sample. The wavelength of IR radiation that is absorbed

is specific to the vibrational or rotational frequencies of chemical bonds within the molecule. Therefore, the absorption peaks in FTIR provide information on the chemical bonds present in the sample.

The AX samples were analyzed before and after chemical modification using an FTIR spectrophotometer (Frontier, PerkinElmer, Waltham, MA, USA) in attenuated total reflection (ATR) mode in the spectral range of 4000-400  $\text{cm}^{-1}$  at room temperature. Spectra were obtained with a resolution of 4  $\text{cm}^{-1}$  and using 16 scans for each spectrum. Measurements were made in duplicates.

### 3.3.4 NMR

NMR uses a magnetic field to cause polarization (alignment) of the nuclear spins of the atoms in the sample. Radio waves can be used to manipulate the magnetized moment through specific pulse sequences and delays. When perturbed by radio waves, the magnetic moment of each nuclei precesses at a characteristic frequency that is related to the chemical environment they are in. A Fourier transform of the obtained data results in the NMR spectra that are commonly seen, such as in Figure 3.4. Specific criteria need to be met by the nuclei being observed for nuclear magnetic resonance to occur, some of the most common isotopes that can be used for NMR are  $^1\text{H}$ ,  $^{13}\text{C}$  and  $^{31}\text{P}$ .

The molar substitution (MS) was evaluated using  $^1\text{H}$  NMR spectroscopy. The BGE-diol AX hydrolysates used to prepare HPAEC samples were neutralized with  $\text{CaCO}_3$  and freeze-dried. The powder samples were then dissolved in  $\text{D}_2\text{O}$  and filtered to remove any  $\text{CaCO}_3$  salts. Spectra were recorded on a Varian MR-400 MHz spectrometer and the molar substitution (MS) of BGE was calculated from Equation 3.1, where the integral intensity from the signal from the BGE methyl group signal (0.9 ppm) was compared to the signals of  $\alpha\text{-H1}$  (5.2 ppm) and  $\beta\text{-H1}$  (4.5 ppm) from the AX units. Note that each BGE side chain has 3 protons in the terminal methyl group, while arabinose and xylose contain 1 proton on each C1 position.

$$MS = \frac{\int \text{methyl protons of BGE}}{3 \times \int \alpha\text{-H1} + \beta\text{-H1}} \quad (3.1)$$

### Diffusion NMR

To confirm covalent or tightly bound non-covalent BGE content, pulsed-field gradient diffusion NMR was performed on polymeric BGE-diol AX samples dissolved in  $\text{DMSO-d}_6$ . The experiment is described in more detail in manuscript II. In short, a series of NMR spectra were corrected at different magnetic field strengths between 0.18 and 60 G/cm. The experiment allows for measurement of the diffusivity of molecules in the BGE-diol AX solution.



Smaller molecules, such as water or DMSO have a high diffusivity, and with increasing gradient strengths, the intensity of their signals in the spectra will decay steeply. Larger molecules such as polysaccharides, will have diffusivity orders of magnitude lower and therefore, be affected less by the gradient increase. A diffusion NMR spectra obtained using the DgctseSL sequence is shown in Figure 3.4, the DMSO signal at 2.5 ppm disappears at a much faster rate compared to the other signals in the spectrum which are associated with polymeric molecules.

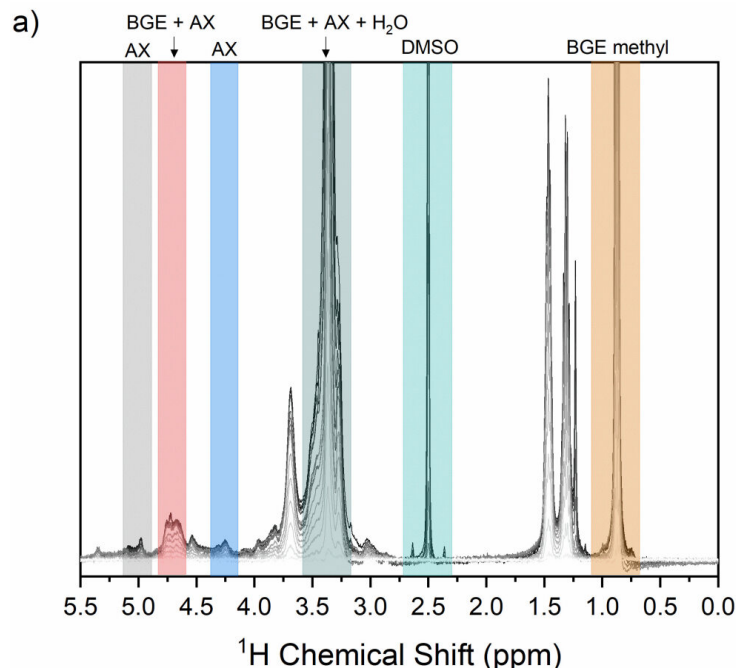


**Figure 3.4:** A  $^1\text{H}$  NMR spectra from BGE-diol AX. The overlaid spectra represent measurements made at different field gradients for diffusion NMR

### 3.3.5 DMA

In DMA, a small oscillatory force (represented as a sinusoidal wave) is applied to the sample. The material's response to deformation provides information about the material's viscoelastic properties [73]. A purely elastic material has its stress and strain completely in phase, while a purely viscoelastic material has a phase lag of  $90^\circ$  between its stress and strain response [73]. Polymers are viscoelastic materials - their properties are a combination of their elastic and viscous responses which can be probed by DMA. The storage modulus ( $E'$ ) representing the elastic properties is obtained from

$$E' = \frac{\sigma_0}{\varepsilon_0} \cos \delta \quad (3.2)$$

and the loss modulus - representing the viscous response is obtained from

$$E'' = \frac{\sigma_0}{\varepsilon_0} \sin \delta \quad (3.3)$$

where  $\sigma_0$  and  $\varepsilon_0$  are the amplitudes of the stress and strain sinusoidal wave, respectively, and  $\delta$  is the phase lag between the stress and strain responses.

As a polymeric material undergoes relaxation at its  $T_g$ , there is a sharp drop in  $E'$  and a rise in  $E''$  as the material softens and shows increased liquid-like flow behavior [74].

Dynamic mechanical properties were measured on a Q800 DMA (TA Instruments, U.S.) in film tension mode. For temperature sweep experiments, the samples were equilibrated at -130 °C for 5 min. Then, measurements were made with a heating rate of 3°C/min, frequency of 1 Hz and an amplitude of 8  $\mu$ m. The samples were conditioned in a climate chamber at 25 °C and 55% relative humidity for at least 24 h before measurements.

## 3.4 Thermomechanical characterization

### 3.4.1 DSC

DSC measures the heat capacity of the material as a function of temperature. When a change in material property occurs, there is typically an exotherm or endotherm associated with the process. For example, the melting of crystalline polymers requires energy to break down the ordered structures. As a result, more heat flow is needed to increase the temperature of the polymer at its  $T_m$  and the DSC pattern shows an endothermic peak. Changes in the material associated with a change in states such as melting, condensation, and evaporation are considered first-order transitions.

The  $T_g$  of a material is not associated with any latent heat or an abrupt change in volume [75]. The  $T_g$  is therefore considered as a second-order transition. In a DSC pattern, the  $T_g$  is observed as a gradual change in the slope as the material starts to relax and increase in volume [75].

DSC was measured using a DSC 2 STARe system (Mettler Toledo, Switzerland), under N<sub>2</sub> flow of 50 mL/min. Samples were equilibrated at -80°C for 5 min and then heated to 170°C at a rate of 20 °C/min. A cooling and a second heating cycle followed – cooling to -80 °C at 20 °C/min, then to 170 °C at 20 °C/min.

### 3.4.2 TGA

The onset of degradation of the materials were studied using TGA. The changes in mass of the sample with increasing temperature were measured. Samples were measured using a TGA/DSC3+ Star System (Mettler Toledo, Switzerland).

Samples were heated from 30 °C to 500 °C at a rate of 10 K/min under a N<sub>2</sub> flow of 60 mL/min.

### 3.4.3 Tensile testing

To measure the stiffness and ductility of the material, a tensile test was performed to obtain the stress and strain response of the material above the elastic strain region.

Film samples were conditioned in a climate room at  $23 \pm 1$  °C at  $50 \pm 2.5$  % relative humidity (RH) for over 72 h before testing. Measurements were conducted in the same climate using a 5944 Universal tensile testing machine (MA, USA) in accordance with ASTM D882. At least 5 replicates were tested for each sample. Straight rectangular specimens were cut out from sample sheets, having a cross-section of  $2 \times 0.1$  mm<sup>2</sup> and a length of 30 mm. A gauge length of 15 mm was used. A preload of 0.05 N and crosshead speed of 30 mm/min was used.

## 3.5 X-ray and neutron scattering

### 3.5.1 SANS

For data produced in manuscript I, SANS data was collected at the Sans2d beamline at the ISIS pulsed neutron and muon source, Rutherford Appleton Laboratory (RAL, Didcot, UK). Samples were placed in 2 mm path length quartz cells, and loaded onto sample racks with temperature controlled to 25°C.

Data averaging, transmission correction, normalization and solvent subtraction was performed using the ISIS SANS Reduction GUI on the Mantid workbench 6.5 to obtain the scattering intensity  $I(Q)$  in absolute scale (cm<sup>-1</sup>). Subtraction of incoherent scattering background and analysis of power law exponent of scattering curve was performed in Matlab software. Fitting of data to the Guinier fit was performed using SasView 5.0.5.

### 3.5.2 X-ray scattering

For data produced in manuscript II, SAXS and WAXS measurements were conducted on a SAXSLAB Mat:Nordic (Denmark) benchtop instrument with a Cu K $\alpha$  radiation source, covering a  $Q$  range from 0.01-2.7 Å<sup>-1</sup>. The detector distance was 477 mm and 126 mm for SAXS and WAXS, respectively.  $q$ -calibration was performed using silver behenate powder. Modified BGE-DiolAX compression molded samples were mounted between two Kapton films and clamped to a solid sample holder, while the AX0.9 sample was solvent casted and measured as a self-standing film.

For temperature step SAXS experiments, the BGE-diol AX films placed between Kapton films to reduce warpage and secured onto a Linkam300 heating stage. An external thermocouple was secured to measure the temperature of the surface of the film in addition to the temperature of the heating stage. 12 temperature settings were used between 25 °C and 200 °C, corresponding to 25°C to 120°C on the sample surface. Each sample was equilibrated for 15 min at each temperature before measurement with 600 s exposure time.

For both measurement methods, the direct beam intensity was measured to determine the absolute intensity of the measured scattering patterns. Data reduction was done with the SAXSGUI software (version 2.27.03). Thickness correction and subtraction of the Kapton background were done using Matlab software program. Peak fitting to various lineshapes were performed using the Fityk software (version 1.3.1).

## 4 Results and Discussion

### 4.1 Neutron scattering studies of wood xylan and dialcohol xylan dispersions

The first section of the thesis explores the hypothesis that the dispersibility of xylans can be improved through increasing the flexibility of the xylose backbone, irregardless of their chemical compositions. The results are based on data presented in manuscript I.

The dispersibility of xylan is driven by the content of side groups substituted on the xylan backbone, with an improvement at higher degrees of substitutions, which decreases the tendency to self-aggregate [7, 10]. As such, the chemical composition of the xylan materials were characterized by HPAEC and an uronic acid analysis protocol. The results are shown in Table 4.1.

**Table 4.1:** *Composition and molecular weight of xylans used in the study*

Abbreviation	Relative carbohydrate composition (wt%)						Uronic acid (mol%)	$M_w$ (g/mol)	$\bar{D}$
	Xyl	Glu	Gal	Ara	Man	Rha			
X1	99	0	0	0	0	0	8	14000	2.5
X2	96	<2	<2	<1	0	0	12	24000	1.3
X3	99	0	<1	<1	0	<1	10	49000	2.5

#### 4.1.1 Xylan dispersibility in water

By visual inspection, none of the xylans produce a transparent dispersion in water (Figure 4.1a-c). However, the degree of turbidity varies between the samples with the X2 being partially translucent - it is still possible to see through the vial.

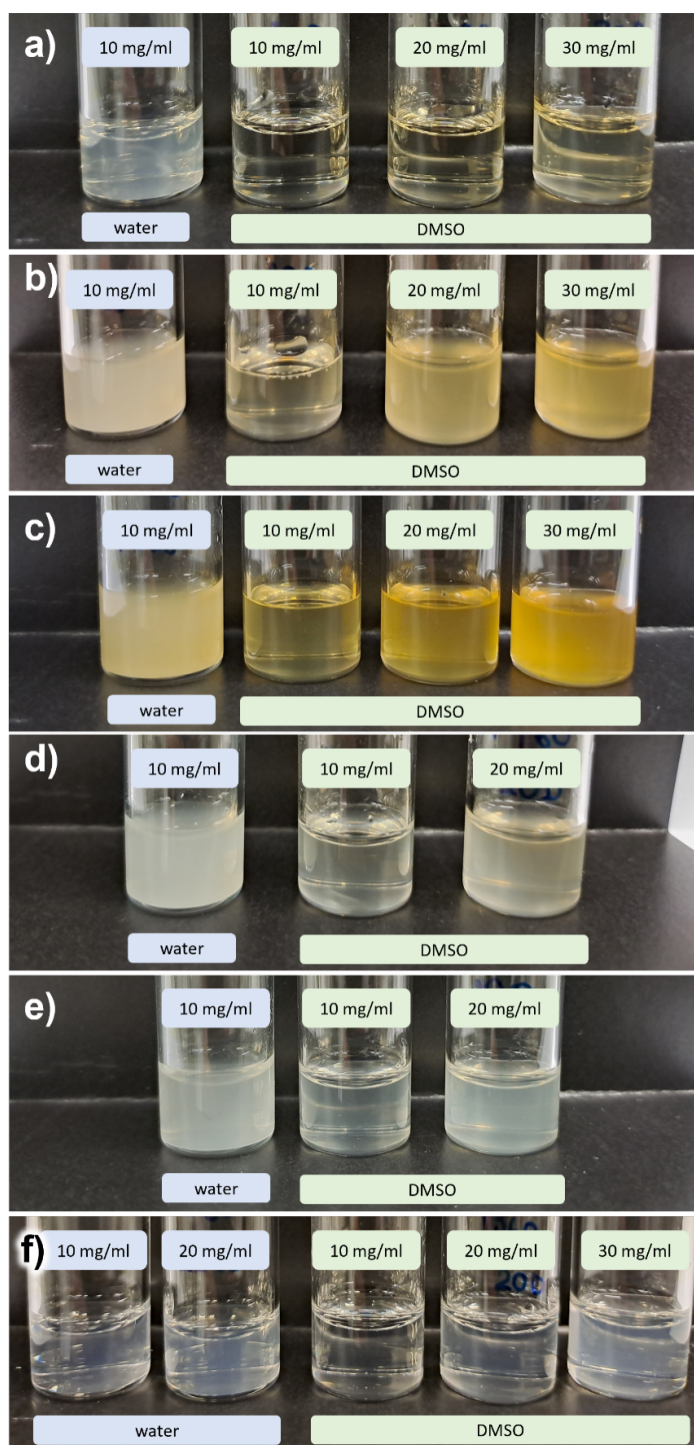


**Figure 4.1:** Images showing the visual appearances of xylan and dialcohol xylan dispersions in water and DMSO at different concentrations. X2 (a), X1 (b) and X3 (c) solutions dispersing in  $H_2O$  and DMSO at concentration of 10 mg/ml and 10-30 mg/ml for  $H_2O$  and DMSO, respectively. DalX1-60 (d), DalX1-75 (e) and DalX2-60 (f) dispersed in  $H_2O$  at concentration range between 10-20 mg/ml and DMSO at concentration between 10-30 mg/ml

The X2 water dispersion was therefore of interest for SANS investigation, and a dispersion in D<sub>2</sub>O was made. The X2 scatters well in D<sub>2</sub>O at 10 mg/ml and the collected SANS data is shown in Figure 4.2.

**The high  $q$  region ( $> 0.09 \text{ \AA}^{-1}$ )** is shown as the rightmost region in Figure 4.2. In this region, a  $q^{-1}$  power law scaling of the scattering was observed, which is typical for stiff polysaccharides with rod-like segments [76].

**At intermediate  $q$  ( $0.02 < q < 0.1 \text{ \AA}^{-1}$ )**, a power scaling exponent of 3.3 was observed. At exponents between 3 and 4 we are likely probing the surface scattering of a dense and compact 3D object. As an exponent of 4, which would be scattering from a smooth surface, was not recovered, the surface of the 3D structure is rough, with a surface fractal dimension  $D_s = 2.7$  given by  $q^{(6-D_s)}$  [70]. This is logical, as at  $0.02 < Q < 0.1 \text{ \AA}^{-1}$ , the size of structures we are probing is in the 1 – 30 nm range and the compact structure observed is likely to be a cluster from collapsed xylan chains. The stiff xylan chains are unlikely to be able contort into compact 3D structures with a perfectly smooth surface.

**At lower  $Q$  values ( $< 0.01 \text{ \AA}^{-1}$ )**, an exponent of 1.4 was observed which is related to the fractal dimension of the resulting aggregates of multiple xylan chains. Hence it is plausible that these collapsed xylan chains form larger structures involving multiple chains, which are themselves not particularly dense, as is suggested by the exponent of 1.4.

The absence of any plateau in the low  $q$  region would indicate that these aggregates are larger than the SANS detection range. The Guinier regime takes place at  $qR_g < 1$  [65, 70, 76]. With the configuration used at Sans2d, data can be obtained down to  $q = 0.002 \text{ \AA}^{-1}$  depending on the scattering intensity of the sample at the lowest  $q$  points. Therefore, the largest detectable aggregate size for SANS in this work is approximately 50 nm.

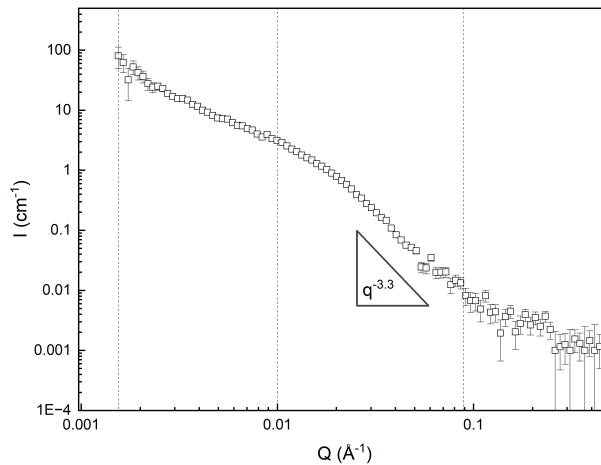


**Figure 4.2:** SANS curve of X2 in D<sub>2</sub>O at a concentration of 10 mg/ml

### 4.1.2 Xylan dispersibility in DMSO

Pre-swelling with water, followed by dispersion in DMSO results in a better solvent environment for xylans [10, 17]. This is well reflected in the transparent visual appearance of X2 (Figure 4.1a), and the translucent appearances of X1 and X3 (Figure 4.1b,c) in DMSO at 10 mg/ml. With increased concentration, the formation of aggregates leading to increasingly turbid dispersions were observed in all samples.

SANS measurements were performed for X1, X2 and X3 at concentrations of 10, 20 and 30 mg/ml in DMSO-d<sub>6</sub>. SANS data from the 20 mg/ml samples (Figure 4.3) were chosen for detailed analysis, as they had better scattering statistics than the 10 mg/ml samples.

**In the high  $q$  region ( $> 0.09 \text{ \AA}^{-1}$ ),** the  $q^{-1}$  scaling from the rod-like segments are observed for X1, X2 and X3 similar to when they were dispersed in water.

**In the intermediate  $q$  region ( $0.01 < q < 0.09 \text{ \AA}^{-1}$ ),** the SANS curve for X1 and X2 exhibited power law exponents of 1.7 - 1.8. Power law exponents of 1.7 - 1.8 represent scattering from swollen polymer chains in a good solvent and the power law exponents are the inverse of their Flory exponent  $v$ . In the case of X1 and X2,  $v = 1/1.7 = 0.588$  (Figure 4). The X3 has an exponent close to 2, thus behaving more as a chain in a theta solvent with  $v = 0.5$  [65, 70].

The pronounced shoulder of the X1 and X2 at  $q = 0.01 \text{ \AA}^{-1}$  could be used to approximate a  $R_g$  of individual xylan chains using a Guinier fit, giving as 8 and 11 nm, respectively. This agrees with the higher  $M_w$  of X2 compared to X1.

**In the low  $q$  region ( $< 0.01 \text{ \AA}^{-1}$ ),** X1 and X2 showed a gradually increasing upturn, ending in a power law exponent of 4. These upturns are indicative of scattering from larger aggregates as discussed earlier. The tendency towards  $q^{-4}$  shows that the swollen xylan chains aggregate to form large highly compact structures. The curve of the X3 exhibited a sharper increase at the start of the upturn than X1 and X2, which could indicate a larger population of large aggregates.

The xylans were in good or theta solvent environments. The observation is in agreement with the improved dispersibility observed in the macroscopic scale. However, it seemed that they still aggregate even for the most well dispersed sample X2. Diluting to a concentration of 10 mg/ml does not change the scattering features at low  $q$  (not shown here). This tendency could be an intrinsic property due to the molecular structure of xylans, similar to those observed in xyloglucans [76, 77].

When increasing the concentration to 30 mg/ml (Figure S3), the xylans showed an increased power law exponent in intermediate  $q$ , independent of xylans (thus regardless of composition and molar mass), which indicates a larger increase in self-interaction as a function of concentration. AX measured by Petermann et al. showed no changes in the intermediate  $q$  exponent even at 135 mg/ml [65]. The mechanism of association for xylans are more concentration dependent, as only



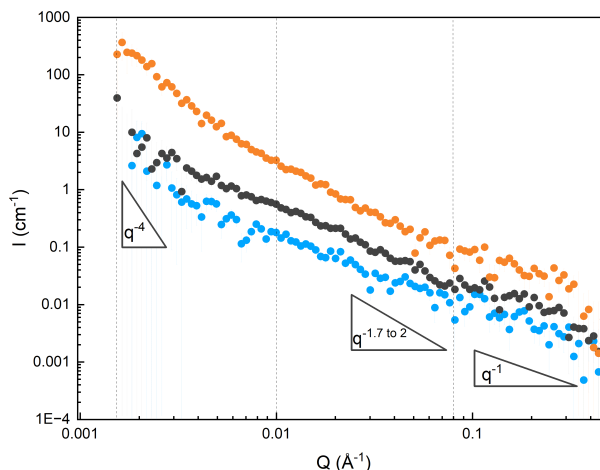


**Figure 4.3:** SANS scattering curve for X1 (blue circle), X2 (black square) and X3 (orange triangle) xylan solutions in DMSO-d6 at concentration of 20 mg/ml. The intensities have been shifted for X2 and X3 for ease of viewing.

**Table 4.2:** Degree of oxidation and molecular weights of the dialcohol xylans

Sample	Deriving from	Degree of oxidation (%)	$M_w$ (g/mol)	Polydispersity
DalX1_75	X1	77	10500	2.5
DalX1_60	X1	63	12200	2.8
DalX2_75	X2	75	18100	2.0

a three-fold increase in concentration to 30 mg/ml resulted in the formation of large visible aggregates.

In summary, the macroscopic appearances of the xylan dispersions confirm that the substituent content is decisive for controlling the dispersity in both water and DMSO. The X2, which contained 12 % uronic acid group content was less turbid when dispersed in water and could be dispersed to form a transparent dispersion in DMSO. Small differences in the macroscopic appearances were found between X1 and X3 in either solvent despite X1 and X3 having the largest difference in molar masses. Both X1 and X3 were turbid when dispersed in water and translucent in DMSO. From SANS data, X1, X2 and X3 all showed good solvent or theta solvent behavior in DMSO confirming that DMSO acts as a better solvent for xylans than water. Despite being in a good solvent however, the xylans all formed aggregates with structures larger than the SANS detection limit of 50 nm being found in all samples.

### 4.1.3 Dialcohol xylans in water and in DMSO

The nomenclature, DO and  $M_w$  of the prepared dialcohol xylans are shown in Table 4.2.

### Dialcohol xylans from X1

By visual inspection, DalX1-60 formed a fully turbid dispersion in water, and a slightly turbid dispersion, with less color when dispersed in DMSO at 10 mg/ml (Figure 4.1 d). Upon increasing the concentration to 20 mg/ml, the DMSO dispersion turned fully turbid.

Likewise, the DalX1-75 dispersion was turbid in water and formed a slightly turbid, colorless dispersion in DMSO at 10 mg/ml (Figure 4.1e). At 20 mg/ml in DMSO, a turbid dispersion was again obtained.

SANS measurements were performed for DalX1-60 and DialX1-75 at concentrations of 10 and 20 mg/ml in DMSO-d<sub>6</sub>. The SANS curve of DalX1-60 in DMSO-d<sub>6</sub>, 10 mg/ml is shown in Figure 4.4.

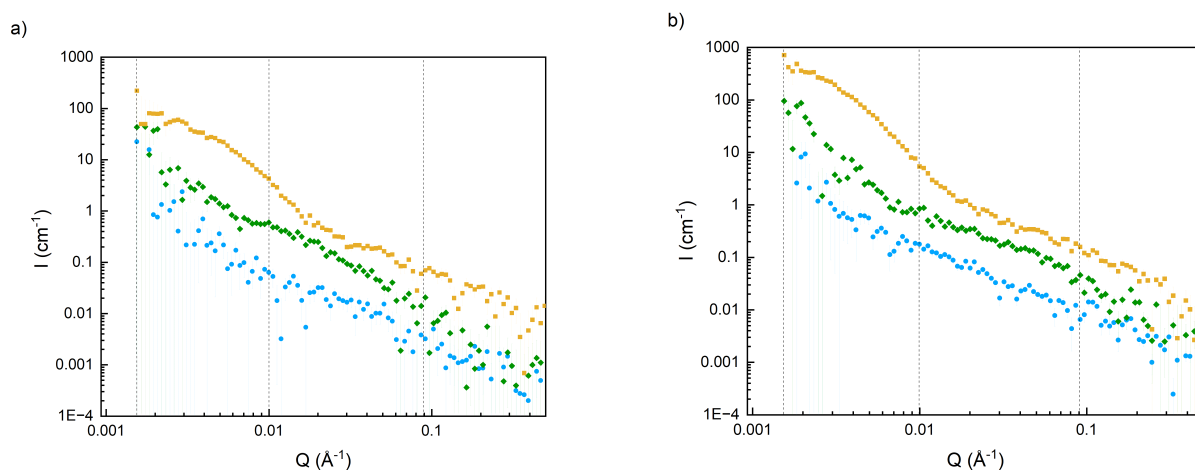


**Figure 4.4:** SANS scattering of X1 (blue circle) and DalX1-60 (green triangle) and DalX1-75 (yellow square) oxidation at concentration of 10 mg/ml (a), 20 mg/ml dispersed in DMSO-d<sub>6</sub> (b). The intensities are shifted for DialX1-60 and DialX1-75 for ease of viewing.

**In the high  $q$  region ( $> 0.09$  Å<sup>-1</sup>),** the scattered curve still follows the same  $q^{-1}$  scaling, as the non-modified sample. There does not seem to be a large change in the  $q$  values where the intensity deviates from a  $q^{-1}$  scaling, which is correlated to the persistence length. Therefore, it seems the persistence length of the modified sample is not significantly changed.

**In the intermediate  $q$  region ( $0.01 < q < 0.09$  Å<sup>-1</sup>),** the scattering curve shows a power law exponent of 1.8 - similar to its unmodified counterpart, X1. This indicates a favorable solvent environment for the modified DialX1-60 as well. The shoulder at  $q = 0.01$  Å<sup>-1</sup> can be fitted to a Guinier  $R_g$  of 8 nm. Compared to X1, the fitted size is not significantly different, but the intensity is higher for the DalX1-60. This suggests that there was a larger population of DalX1-60 solubilized and observed as individual units.

**In the low  $q$  region ( $< 0.01$  Å<sup>-1</sup>),** a low  $q$  upturn is observed which ends in a

power law exponent of 4, characteristic of scattering from larger aggregates [70].

When the concentration was increased to 20 mg/ml (Figure 4.4b), the scattering of DalX1-60 overlaps almost completely with X1 at 20 mg/ml. Therefore, the DalX1-60 seems better solubilized at low concentrations but behaved similarly as the non-modified counterpart (X1) when the concentration is increased to 20 mg/ml.

The scattering curve of DalX1-75 in DMSO-d6 is shown in (Figure 6a-b). The scattering curve/pattern is comparable to X1 and DalX1-60 in the high  $q$  region.

**In the intermediate  $q$  region ( $0.01 < q < 0.09 \text{ \AA}^{-1}$ ),** the scattering curve shows signs of a shoulder around  $q = 0.02 \text{ \AA}^{-1}$ . The curve is obfuscated by a steep upturn, however the location of the shoulder should be similar to that of DalX1-60 - with an associated  $R_g$  of 8 nm.

**In the low  $q$  region ( $< 0.01 \text{ \AA}^{-1}$ ),** the steep upturn forms another shoulder fitted to a  $R_g$  of 36 nm. Increasing the concentration from 10 mg/ml to 20 mg/ml results in a stronger intensity for the second peak, even after normalizing the scattering intensity for concentration. This shows that increased aggregation occurs with concentration but the structures formed are small. This suggests that some improvement in dispersibility is achieved at DO close to 75.

By macroscopic appearance it remains inconclusive whether DalX1-60 and DalX1-75 are better dispersed than their unmodified counterparts. At 10 mg/ml, X1, DalX1-60 and DalX1-75 are slightly turbid, and at 20 mg/ml, a strong concentration dependent aggregation was observed. DalX1-60 in dispersion does not significantly change when observed with SANS. While changes were observed for DalX1-75 where SANS suggested a partial reduction in aggregate sizes, and therefore improved dispersibility. It is possible that the improvement is inhomogeneous, with the larger aggregates not being modified to the same extent as smaller ones and hence not having equally improved dispersibility.

## Dialcohol xylans from X2

DalX2-60 dispersed faster in water and the appearance of the dispersion was clearer than the unmodified X2 in water at 10 mg/ml (Figure 4.1f). When dispersed in DMSO, DalX2-60 was transparent at 10 mg/ml but turned turbid with increasing concentration, similar to the X2 in DMSO.

The scattering curve for DalX2-60 in D<sub>2</sub>O showed similar patterns to that of the X2 in D<sub>2</sub>O. But the scattering for DalX2-60 was concentration independent, indicating that the solvent interaction or aggregate nanostructure is independent within the concentration range studied.

**In the intermediate  $q$  ( $0.01 < q < 0.1 \text{ \AA}^{-1}$ ) region,** the power law exponent of DalX2-60 was reduced for the D<sub>2</sub>O dispersion. The X2 in D<sub>2</sub>O had an exponent of 3.3 (Figure 4.2), whereas the DalX2-60 had an exponent of 2.7 (Figure 4.5). The results therefore indicate that the solvent interaction has been improved with

the modification.

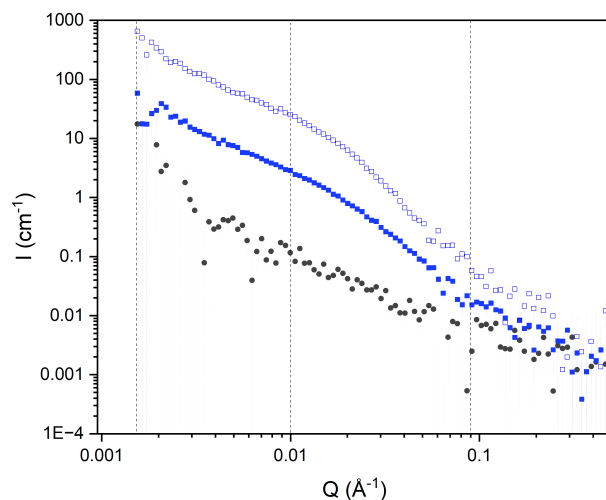


**Figure 4.5:** SANS scattering curve of X2 (black circle) and DalX2-75 (blue circle) in D<sub>2</sub>O (hollow symbol) and DMSO-d<sub>6</sub> (solid symbol) at concentration of 10 mg/ml. The intensities have been shifted for DalX2-75 in D<sub>2</sub>O and DMSO-d<sub>6</sub> for ease of viewing.

In the low  $q$  region ( $< 0.01 \text{ \AA}^{-1}$ ), a  $q^{-1.4}$  exponent correlated to larger aggregate structures was again observed. The general features of the low  $q$  scattering curve are similar with X2, the system still seem to form similar aggregate structures after modification.

When dispersed in DMSO-d<sub>6</sub>, the scattering curve of DalX2-60 was changed significantly after modification.

In the intermediate  $q$  ( $0.01 < q < 0.1 \text{ \AA}^{-1}$ ) region, the power law exponent was increased to 2.7, compared to 1.8 for the X2. An exponent of 2.7 indicates scattering from a collapsed chain under poor solvent environments [70], in contrast to 1.8 which shows a chain in a good solvent. At lower  $q$  values, the same  $q^{-1.4}$  decay was observed showing that the larger aggregate structure is similar to the DalX2-60, and by extension, X2 in D<sub>2</sub>O (Figure 4.5)

#### 4.1.4 A summary of the first section

Probing xylans in water and DMSO using SANS show that the xylans readily aggregate even in favorable solvent conditions. There may be several association mechanisms involved – some of which are concentration dependent. The content of side group substituted on xylan is concluded to be the main factor in determining dispersibility in the nanometer scale.

The first hypothesis was that the oxidation and reduction could help to improve the dispersibility of xylans. The conclusion is that the effect seems to differ based

on the properties of the starting xylan material. In the case of the X1, going to a high DO such as 75 % resulted in a reduction of aggregate sizes. However, the effect was not significant enough to obtain a macroscopically transparent dispersion.

In the case of X2, the solvent interaction with water was improved and the dispersion appeared more translucent. However, the solvent interaction in DMSO was worsened when probed with SANS.

The hypothesis was partially correct in that the solvent interactions could be changed. And there is some scope to tune for dispersibility in specific solvents, however, the improvements are not sufficient to break down all micron-sized aggregates. Therefore, dialcohol xylans will need to be further functionalized with other functional groups to obtain full dispersibility.

## 4.2 Nanostructure and thermomechanical properties of modified AX films

The second section of the thesis explores thermomechanical properties, such as  $T_g$ , Young's modulus and ductility, of oxidized-reduced-etherified AX materials in relation to their starting chemical and structural properties.

The hypothesis is that the starting molecular structure of AX has an affect on the success of the modification. This could be indirectly through different reactivity and solubility during the reaction. Or directly, where the structural features such as crystallinity and branching density directly control the property of the final product. The thermomechanical properties are compared and the structures of the melt compressed films were studied using small and wide angle X-ray scattering.

### 4.2.1 Chemical composition of extracted AX from wheat bran

The monosaccharide composition of the extracted AX fractions are presented in Table 4.3. The majority of glucose content in AX0.3 were  $\beta$ -glucans, accounting for 14 wt% of the material. As such, further purification using  $\beta$ -glucanase, to reduce the glucose content was performed. The purified AX0.3 showed a lower amount of glucose, indicating that  $\beta$ -glucan had co-precipitated during the fractionation. The purification and reprecipitation also further lowered the ara:xyl ratio in AX0.3.

The major compositional difference, apart from arabinose and xylose, between the samples (AX0.3, AX0.5 and AX0.9) is the amount of insolubles of AX0.3 (15 wt %) compared to AX 0.5 and AX 0.9 (4 and 5 wt% respectively). Insolubles here include lignin that is not soluble under acid conditions (ASL), but also other compounds that were not hydrolyzed. The relatively higher percentage of insolubles, as observed in the starting material AX0.3, was only observed in the first batch used. A second enzymatic purification was performed (unpublished data) and the insoluble content was only 6 %wt. The insoluble content also do not carry over to the modified sample. They are likely purged away during the modification, or there was an outlier in this specific measurement sample.

### 4.2.2 Results of periodate oxidation and sodium borohydride reduction

The DO was estimatated by following peridate consumption through the absorption band in UV-Vis at 290 nm. 100 %, 84 % and 88 % of added sodium periodate were consumed for AX0.3, AX0.5 and AX0.9, respectively. These corresponded to DO of 25 %, 21 % and 22 %. These dialcohol AX are named subsequently as Diol AX.

**Table 4.3:** Monosaccharide composition in wt %, mass of insolubles and acid soluble lignin (ASL) of AX0.3 before and after addition of  $\beta$ -glucanase, AX0.5 and AX0.9. n.d. – not detected, below detection limit of method.

Component (wt %)	AX0.3 (before $\beta$ -glucanase)	AX0.3	AX0.5	AX0.9
Arabinose	23	17	29	41
Rhamnose	n.d.	n.d.	n.d.	n.d.
Galactose	2	1	3	3
Glucose	15	8	8	3
Xylose	41	56	53	44
Mannose	n.d.	n.d.	n.d.	n.d.
Insolubles	11	15	4	5
ASL	9	3	3	4
Ara:xyl ratio	0.56	0.30	0.55	0.93

### 4.2.3 Results of BGE substitution

The successful modification of BGE onto Diol-AX (BGE-diol AX) was confirmed by FTIR, HPAEC and  $^1\text{H}$ NMR.

In FTIR, the presence of BGE side chains was observed as an increased intensity in the -CH<sub>2</sub> and -CH<sub>3</sub> absorption band between 3000-2800 cm<sup>-1</sup>. A decrease of the band at 1630 cm<sup>-1</sup> was interpreted as a decrease in hydrated water signals according to a work by Nylander et al. [78]. A stronger absorption band was also observed at 1465 cm<sup>-1</sup> (CH<sub>2</sub>- bending), relative to the unmodified samples, and a new peak at 740 cm<sup>-1</sup> (C-H, long-chain methyl rock), which comes from the BGE reagent.

The results of the characterization of the molar substitution (MS) by  $^1\text{H}$ NMR and indirectly by HPAEC is shown in Table 4.4. As HPAEC only detects unmodified monosaccharides, the mass recovery difference between unmodified AX and its corresponding BGE-diol AX can be approximated to the mass ratios between BGE and AX. There is some uncertainty whether all BGE is cleaved from AX during hydrolysis, as a BGE-xylose or BGE-arabinose unit would also have a different retention time and not be detected.

In  $^1\text{H}$ NMR, hydrolysates of BGE-diol AX were measured.  $\alpha$ -arabinose and  $\beta$ -xylose have their H1 chemical shift peaks at 5.2 and 4.5 ppm respectively. BGE has terminal methyl groups which are located upfield with a chemical shift of 5.2 ppm. BGE-diol AX0.3, 0.5 and 0.9 have similar substitutions between 0.9 and 1.1.  $^1\text{H}$ NMR were also performed on polymeric BGE-diol AX materials dissolved in DMSO-d<sub>6</sub>. MS determined from polymeric samples had a higher degree of uncertainty as BGE side chains contain a downshifted proton close to the AX H1 peaks when attached. Such analysis gives a MS between 0.8 and 1.2 for all samples (unpublished data).

**Table 4.4:** Data on composition of modified BGE-diol AX materials including: DO, unmodified AX content in wt%, and molar substitution measured by  $^1\text{H}$ NMR on hydrolysates.

Material by HPAEC (wt%)	Degree of oxidation (DO %) MS by $^1\text{H}$ -NMR	Unmodified AX	
BGE-diol AX0.3	25	43	0.92
BGE-diol AX0.5	21	38	0.95
BGE-diol AX0.9	22	35	1.1

#### 4.2.4 Diffusion NMR of BGE-diol AX

Pulsed-field gradient diffusion NMR was used to confirm the absence of freely diffusing BGE molecules. The data from the diffusion experiments of the BGE-diol AX0.5 sample can be seen in Figure 4.6. In Figure 4.6, a series of DgcsteSL spectra with increasing  $k$  and the component from which each signal originates from are shown. Plotting the log of the signal integral intensities for each spectrum against the  $k$ -value produces Figure 4.6b, where  $k$  is the attenuation constant proportional to the square of the gradient strength.

The slope is related to the self diffusion coefficient through the Stokes-Einstein equation, which will not be discussed here. The signals denoted as AX, BGE, BGE+AX should decay slowly and with similar rates as we expect them to be polymeric and covalently bonded. DMSO should decay rapidly and BGE+AX+H<sub>2</sub>O should have a fast and a slow decaying component. As the plot in Figure 4.6b agree with our predictions, it is implied that the reaction was successful.

#### 4.2.5 Compression molded films of BGE-diol AX

BGE-diol AX0.3, 0.5 and 0.9 were compression molded into films of 0.1 mm in thickness. The BGE-diol AX0.3 showed macroscopic inhomogeneities, observed as opaque clusters on the film (Figure 4.7a), while the films produced using BGE-diol AX0.5 and BGE-diol AX0.9 were clear and transparent (Figure 4.7b-c). It should be noted that the textures observed on all films are a result of patterns on the Teflon sheet. All three films were flexible and could be bent and folded.

The compression molded films were then tensile tested in a controlled room at  $23 \pm 1$  °C and  $50 \pm 2.5$  % relative humidity. A stress-strain curve for each of BGE-diol AX0.3, 0.5 and 0.9 is shown in Figure 4.8. Films of BGE-diol AX0.9 were characterised by a lower modulus and a high strain at break. Films of BGE-diol AX0.5 had the highest mean tensile toughness (15 MJ/m<sup>3</sup>). They had a Young's modulus close to that of BGE-diol AX0.3, but were more ductile (higher strain at break). Films of BGE-diol AX0.3 were the least ductile of the three



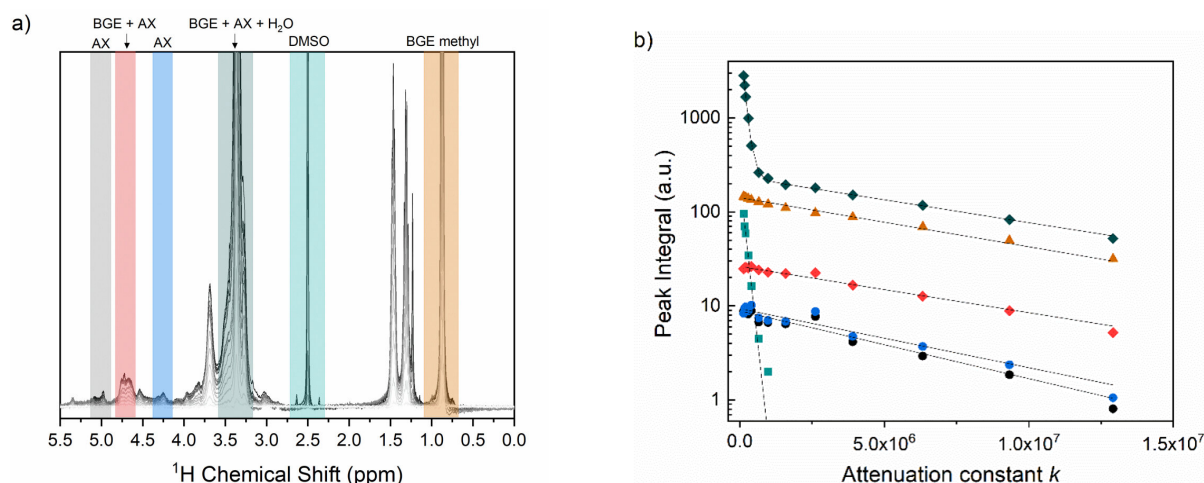


**Figure 4.6:** a) A series of DgcsteSL spectra with increasing  $k$  of the BGE-diol AX0.5 sample. Signal integral intensities used to follow the attenuation with increased  $k$  are highlighted and labeled. b) The integral intensity of the following signals plotted against the  $k$ -value: BGE methyl (orange, triangles), DMSO (green, squares), mixture of BGE, AX sugar ring signals and water (dark green, diamonds), mixture of BGE and AX (overlapped parts of  $\alpha$  ara-H1) (red, diamonds), AX  $\beta$  xyl-H1 (blue, circles), and AX  $\alpha$  ara-H1 (black, circles). Lines denote fitting of single- or bi-exponential decays.

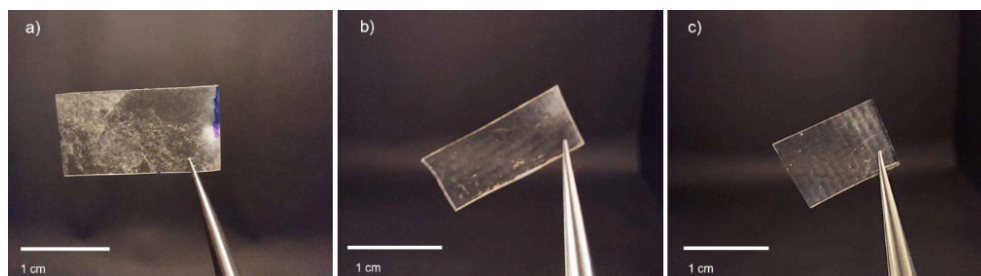


**Figure 4.7:** Images of compression molded films from; a) BGE-diol AX0.3, b) BGE-diol AX0.5, and c) BGE-diol AX0.9, with thickness of 0.1 mm.

modified samples. Several of the tested BGE-diol AX0.3 films underwent failure after yielding, while others could be stretched up to 35% strain with no necking behavior observed. It is possible that macroscopic (Figure 4.7a) and microscopic inhomogeneities, discussed in terms of crystallinity in a later section, were acting as fracture points leading to failure. For comparison, a stress-strain curve of solvent casted AX0.9 is shown in Figure 4.8b. **Note that the both the x and y-axis are on different scales**, as the film of AX0.9 is more brittle than that of BGE-diol AX.

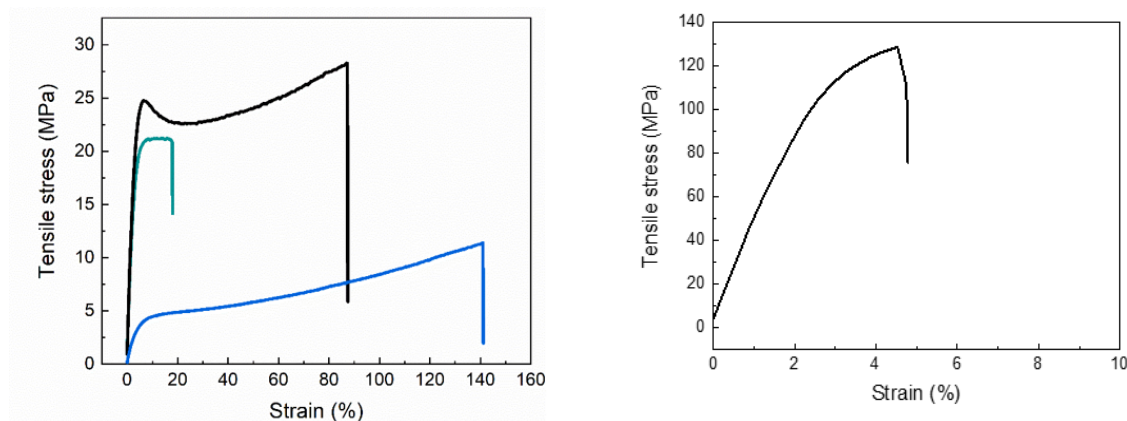


**Figure 4.8:** (a) Stress-strain curves of BGE-diol AX0.3 (green), BGE-diol AX0.5 (black), BGE-diol AX0.9 (blue), (b) a stress-strain curve of solvent casted AX0.9 for comparison ( $x$  and  $y$ -axis are different).

#### 4.2.6 Characterization of BGE-diol AX structures by X-ray scattering

To understand the changes to the polymer structure after modification, X-ray scattering from two instrument configurations (SAXS and WAXS) were combined to produce the curves in Figure 4.9. At low  $q$  ( $< 0.1 \text{ \AA}^{-1}$ ),  $q$ -decays of  $q^{-2}$  for BGE-diol AX0.3, and  $q^{-3}$  for BGE-diol AX 0.5 and 0.9 were observed. The  $q^{-3}$  decay is common in samples exhibiting defects and voids [79–81] which could arise from the melt-compression or solvent casting of films and will not be discussed in detail. The  $q^{-2}$  decay in the BGE-diol AX0.3 films is expected to be a result of larger inhomogeneities, which may be related to the clusters observed macroscopically (Figure 4.7a). At  $1.5 \text{ \AA}^{-1}$ , an amorphous peak was observed for all samples, corresponding to an “average” inter-molecular atom-atom distance.[60, 82] The unmodified AX0.9 has a shoulder at  $0.67 \text{ \AA}^{-1}$ , corresponding to a real space distance of  $9.2 \text{ \AA}$ . All modified samples showed intense correlation peaks at  $0.18 \text{ \AA}^{-1}$  (BGE-diol AX0.3 and BGE-diol AX0.9) and  $0.23 \text{ \AA}^{-1}$  (BGE-diol AX0.5). The correlation peaks correspond to real space distances of  $35 \text{ \AA}$  and  $27 \text{ \AA}$ , respectively.

I expect that the space distances originate from aggregation and subsequent nano-domain formation of BGE side chain and AX backbone rich domains respectively (similar structures to those shown in Figure 2.5). This results in a longer distance between AX backbone chains, thus reducing strong intermolecular interactions between polysaccharide chains. The hypothesis is supported by i) the measured pycnometer density of  $1.4 \text{ g/cm}^3$  for AX0.3 and  $1.26 \text{ g/cm}^3$  for BGE-diol AX0.3. This indicates that the two nano-domains of BGE side chain and AX would have different mass densities – giving rise to observable X-ray contrast, ii) the AX being more hydrophilic than the hydrophobic BGE, reducing

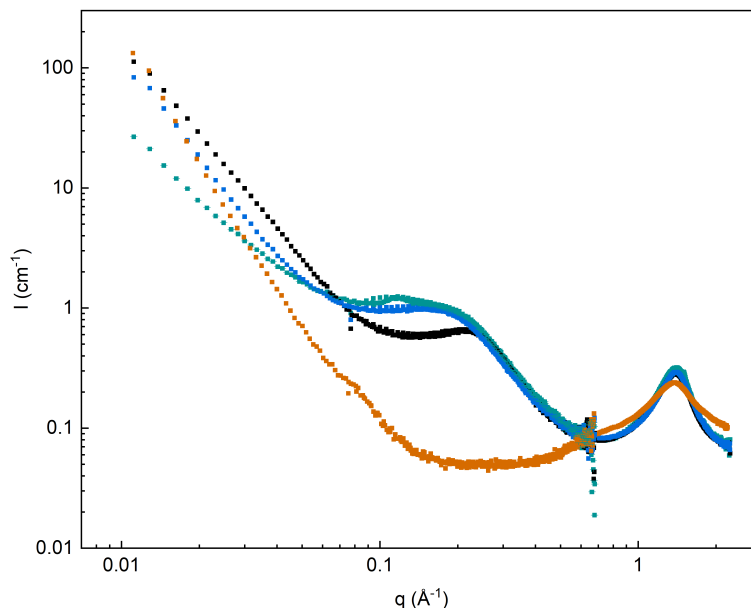


**Figure 4.9:** Combined SAXS and WAXS curve of BGE-diol AX0.3 (green), BGE-diol AX0.5 (black), BGE-diol AX0.9 (blue), and AX0.9 (orange).

their miscibility and iii) the disappearance of the shoulder observed in unmodified AX0.9 in BGE-diol AX0.9; if the shoulder in AX0.9 originates from the spacing between AX chains caused by arabinose side-groups, then their disappearance and replacement by the larger correlation distance from BGE nano-domains is a reasonable explanation.

Native AX0.3 showed Bragg peaks from crystalline chains matching with xylan crystallite diffraction planes in low ara:xyl ratio AX at a  $q$  value of  $0.89 \text{ \AA}^{-1}$  ( $2\theta = 12.4^\circ$ , 101 & 011), and at a  $q$  value of  $1.38 \text{ \AA}^{-1}$  ( $2\theta = 19.1^\circ$ , 110) (Figure 4.10a)[19]. These peaks were altered in BGE-diol AX0.3, which shows peaks at  $1.50 \text{ \AA}^{-1}$  and  $0.12 \text{ \AA}^{-1}$  in the WAXS curve and at  $1.70 \text{ \AA}^{-1}$  in XRD measurements (Figure S5). These peaks do not match with those from a xylan crystallite. It was also observed that the peak at  $0.12 \text{ \AA}^{-1}$  becomes more pronounced upon melt compression. The peak at  $1.70 \text{ \AA}^{-1}$  corresponds to a real space distance of  $3.7 \text{ \AA}$ . It could therefore represent small degrees of lateral crystallization within the BGE side chains, The peak centered at  $0.12 \text{ \AA}^{-1}$  represents increased ordering caused by a thermal history, with the real space distance of  $52 \text{ \AA}$  suggesting that it is related to an ordering of the nano-domain spacings. The ordered structures forming, in addition to the  $q^{-2}$  decay at low  $q$  for BGE-diol AX0.3, are potential fracture initiation points which could lead to the low strain at break observed in the tensile tests.

Temperature step SAXS curve in Figure 4.11a showed that the correlation peaks exist at higher temperatures. The data also showed a temperature dependence in both  $q$  and  $I$  of the correlation peaks, corresponding to fluctuations in size and

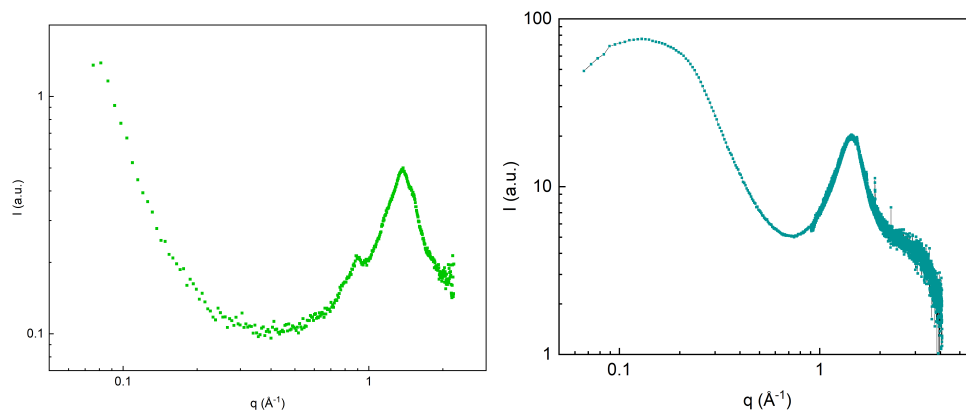


**Figure 4.10:** (a) WAXS curve of unmodified AX 0.3, (b) WAXS curve overlaid with the X-ray diffraction curve of BGE-diol AX0.3

extent of nano-domains. Figure 4.11a shows shoulders that shifted towards lower  $q$ , and increased in intensity between 25 °C and 70 °C. The shift in shoulder and intensity, as a function of temperature, can be explained by swollen nano-domains – likely as a result of residual stresses, and moisture effects (between 1-2 wt% moisture determined by TGA). Then, at higher temperatures, the domains shrink again (shifted to higher  $q$  values with decreasing intensity). The decrease in size and intensity at higher temperatures indicates a gradual decrease in order of the hypothesized nano-domains, as a result of increased mobility of both AX and BGE side chains. By the same reasoning, the BGE-diol AX0.5 being much less influenced by temperature than the BGE-diol AX0.9 could indicate lower mobility in the former.

In addition, the disappearance of the sharper peak at  $0.12 \text{ \AA}^{-1}$  for BGE-diol AX0.3 was observed between the 70 °C and 80 °C curve in Figure 4.11b. This further supports the hypothesis that some sort of ordered structure had formed within the sample, which was subsequently lost at higher temperatures.

## 4.2.7 Thermal properties

### DMA

The DMA data in Figure 4.12 showed that the decrease in storage modulus ( $E'$ ) is dependent on the ara:xyl ratio of the starting material. At the start of the measurement at -130°C, all samples share similarly high  $E'$ . With heating, the moduli reduce with a similar slope for all samples, until  $T = -50 \text{ °C}$ , at which all samples reduce in  $E'$  with a steeper slope, however, BGE-diol AX0.9 softens more with temperature compared to BGE-diol AX0.3 and 0.5. At 20 °C, the values of  $E'$  showed good agreement with tensile testing data, the BGE-diol AX0.9 has a lower  $E'$  of 420 MPa, and the BGE-diol AX0.5 is stiffer than the BGE-diol AX0.3 (740 MPa vs. 570 MPa).  $T_g$  obtained from the first shoulder of the  $E'$  curves gave

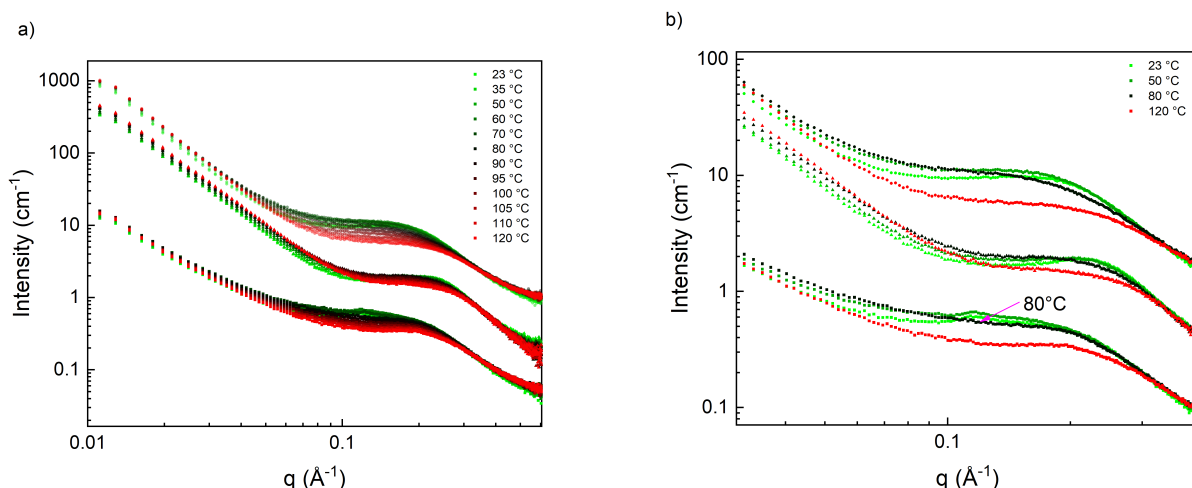


**Figure 4.11:** a) SAXS curve, intensity shifted for viewing, as a function of sample temperature from 25 °C (green), to 120 °C (red) for BGE-diol AX0.9 (top), BGE-diol AX0.5 (middle), and BGE-diol AX0.3 (bottom), b) magnification around the shoulder regions. The curve at 80 °C of BGE-diol AX0.3 is indicated by the arrow.

a  $T_g$  onset of approximately -40 °C for BGE-diol AX0.9 and BGE-diol AX0.3. BGE-diol AX0.5 has a broader shoulder and a higher onset – starting around -30 °C and stretching to 0 °C.

Based on results reported here, and previous work,[83] we observed that the addition of BGE, creates transitions below 0 °C due to the flexibility induced by the side chain. The  $E''$  curves showed three transitions for all BGE-diol AX materials. The first occurs at -75 °C, the second at around -40 °C (and between -30 °C and 0 °C for BGE-diol AX0.5), and the third at 80 °C. At higher substitution values, the transition at -40 °C increases in intensity and becomes the main observable transition [83].

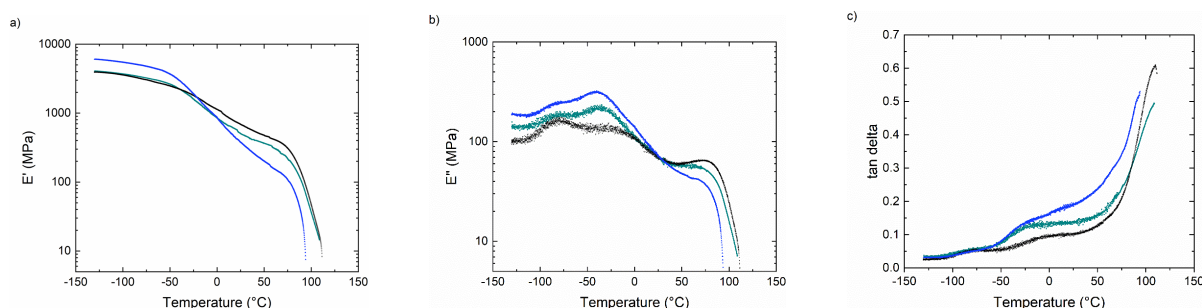


**Figure 4.12:** Representative DMA curves of BGE-diol AX 0.3 (green), BGE-diol AX0.5 (black), BGE-diol AX0.9 (blue): a)  $E'$ , b)  $E''$ , and c) the  $\tan \delta$  as a function of temperature. Measurements performed at frequency of 1 Hz and strain amplitude of 8  $\mu\text{m}$ .

## DSC

DSC plots for the samples are shown in Figure 4.13. The results from the second heating confirm the observations made with DMA measurements. BGE-diol AX samples exhibited two broad transitions at  $-50$  °C and  $90$  °C. These measurements suggested that two separate  $T_g$  are present within the system. Unmodified AX samples did not show any observable transitions within the same temperature range.

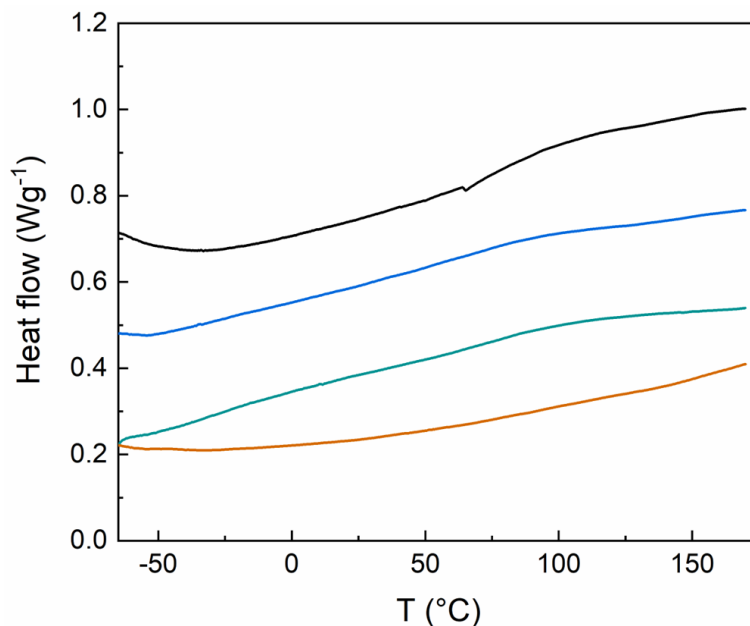


**Figure 4.13:** Second heating DSC curves for AX0.9 (orange), BGE-diol AX0.3 (green), BGE-diol AX0.5 (black), BGE-diol AX0.9 (blue). Endothermal direction is upwards.

Hiller et al.[84] described dynamics within branched nanophase separated poly (n-alkyl acrylates) as exhibiting two  $T_g$ : a lower  $T_{g, \text{side chain}}$  and a higher  $T_{g, \alpha}$  of the entire chain. Between  $T_{g, \text{side chain}} < T < T_{g, \alpha}$ , the polymer exhibits some mobility, but the modulus is kept relatively high by the rigidity of the main chains separating the mobile alkyl domains. The alkyl domains in poly (n-alkyl acrylates) also serve as a form of internal plasticization, bringing  $T_{g, \alpha}$  down as well.<sup>13</sup> Based on structural X-ray data observed for BGE-diol AX samples, as well as DMA and DSC data, the same type of behavior could be reasoned. The BGE chains separate the AX backbone which are typically prone to strong intermolecular bonding which reduces their mobility, and the  $T_g$  reduction is dominated by BGE side chain contributions.

The Young's modulus, and tensile ductility are affected by both the side chains and the rigidity of the native AX that acts as the backbone. It is known that adding more BGE would improve the flexibility of the material. In our study, we



show that the branching ratio of the starting AX could have a similarly significant effect. In the case of BGE-diol AX0.3, X-ray scattering as well as macroscopic inhomogeneities strongly suggest that it is the formation of ordered structures which result in their lower strain at break in tensile. For BGE-diol AX0.5, we observed smaller sizes and response to temperature of the nano-domains. It is unclear why this particular AX structure produces these results. However, the size and lower observed mobility of the nano-domains could be reasonably correlated to a to stretch. Therefore, the rigid AX sections are unable to slide as much as they could in BGE-diol AX0.9 which has a larger domain size.

Stepan et al. also observed similar trends in Young's modulus and ductility in acetylated AX films, although the differences were not as large [85]. Acetyl groups are much shorter than BGE side chains, which could explain the differences observed,

#### 4.2.8 A summary of the second section

The diffusivity, measured by pulsed-field gradient NMR, corroborate the effective reaction of BGE on oxidized and reduced AX, where no or little BGE exist unreacted. A comparison of three fractions of wheat bran AX with different arabinose content were made with regards to the final material thermomechanical properties after oxidation-reduction-etherification modification.

All compositions were shown to produce melt-compressible materials, with the reduction in  $T_g$  of the system determined by the addition of side chain ether groups rather than the main chain properties. We obtained melt processable materials independent of initial arabinose content at similar MS. A significant difference in Young's modulus and ductility of compression molded films were observed, with higher arabinose contents associated with a more ductile modified material.

The discussed model for the behavior exhibited by the system is that of a nanophase separated system consisting of more mobile aggregated side chain domains surrounded by the rigid AX main chain. I observed that different sizes and temperature responses of the nano-domains were AX motif-specific. The findings provide insight on how chemical modification may turn an unmelt-processable polysaccharide into a thermoplastic material and shows that the mechanical properties of the final product can be tuned by controlling the composition of the polysaccharide starting material.





## 5 Conclusions and Future Work

The objective of the thesis was to investigate how the chemical composition of (arabino)xylans affect structures of the materials on the nanoscale. I investigated the conformation and aggregation density of wood xylans in dispersions of water and DMSO. This is relevant for applications such as nanoparticle tuning, modifications or coating. In the second section, I demonstrated how changing the chemical composition of AX results in modified AX melt compressible films with largely varied mechanical properties. And that the variation was explainable by changes in their nanostructures.

The first hypothesis studied in manuscript I was that the oxidation and reduction could help to improve the dispersibility of xylans. The conclusion is that first, the changes are xylan composition specific - different xylan fractions were affected differently. Second, was that the solvent interactions indeed could be changed, and there is some scope to tune for dispersibility in specific solvents. However, the improvements are not sufficient to break down all micron-sized aggregates. Therefore, dialcohol xylans will need to be further functionalized with other functional groups to obtain full dispersibility.

The second hypothesis was that the starting molecular structure of AX has an affect on the success of the modification and on the properties of the modified AX materials. The conclusions were that first, the modification performed well for all the tested AX fractions extracted from wheat bran, even those with lower arabinose substitutions of 0.3. Second, the modified materials' were strongly affected by the chemical compositions of the starting AX. Modified AX0.3 was a more stiff material, while modified AX0.9 had a low modulus and could be stretched up to 140 % strain in tensile. Third, the differences could be in part explained by their nanostructures observed in X-ray scattering. Crystallinity, size of side chain nano-domains and temperature response of the nano-domains were found to be correlated to the starting AX material properties.

For the future, a detailed SAXS/SANS dispersion study on AX extracted from wheat bran is being analyzed and written. Another project involves performing in-situ oxidation SAXS studies, which would enable a real time observation of conformational changes of (arabino)xylans during periodate oxidation. Lastly, I am interested in studying the dynamics of the BGE-diol AX system to better understand which motions are essential for melt processibility. Some preliminary studies using relaxation NMR has been done. Further studies using dielectric spectroscopy and quasi-elastic neutron scattering would be of interest.



# Acknowledgments

We would like to acknowledge Formas – a Swedish Research Council for Sustainable Development, for funding for the PhD project, as well as Vinnova for financial support to the research project. We gratefully acknowledge the Science and Technology Facilities Council (STFC) for access to neutron beamtime at ISIS, and also for the provision of sample preparation, and SANS2D instrument facilities.

We also acknowledge Leide P. Cavalcanti for her assistance at the SANS2D beamline, and the Division of Forest Products and Chemical Engineering at Chalmers for access to carbohydrate analysis. Further, we acknowledge the Chalmers Material Analysis Laboratory (CMAL) for access to X-ray scattering and diffraction instruments, and the research engineer Michal Strach for his help with training and instrument setup.

I would like to express my deepest gratitude to my supervisor Anna Ström for her continuous support and feedback. The work would not have been possible without her encouragement for exploring new ideas, methods and hypothesis. I am also extremely grateful to my co-supervisors Fabrice Cousin, Mikael Hedenqvist and Anette Larsson: Fabrice for his excellent lectures and feedback on scattering techniques, Mikael for his knowledge on polymer testing and for providing access to various testing equipments, and Anette for her knowledge on cellulose derivatives, and for involving me in the FibRe research center.

I would also like to thank my co-authors, especially Patricia, Gain and Tiina for their contributions to the manuscripts the thesis is based on. My examiner Merima Hasani, who I am also very thankful towards for providing access to the Forestry department's laboratories.

Lastly, this first half of the PhD journey would have been substantially less enjoyable without the support and company of my family, friends, and colleagues from TYK, KCK and FibRe. My group members Jakob and Giovanni in particular have become great friends and fairly decent sporting competitors. And it has been great to run into a good old friend, Eliott again at the division.

To another fun and rewarding two years.



# References

- [1] Klemm, D.; Heublein, B.; Fink, H.-P.; Bohn, A. Cellulose: fascinating biopolymer and sustainable raw material. *Angewandte chemie international edition* **2005**, *44*, 3358–3393.
- [2] O'Neill, M. A.; Selvendran, R. R. Hemicellulosic complexes from the cell walls of runner bean (*Phaseolus coccineus*). *Biochemical journal* **1985**, *227*, 475–481.
- [3] Sun, R.; Sun, X.; Tomkinson, J Hemicelluloses and their derivatives. **2004**.
- [4] Scheller, H. V.; Ulvskov, P. Hemicelluloses. *Annual review of plant biology* **2010**, *61*, 263–289.
- [5] Ek, M.; Gellerstedt, G.; Henriksson, G., *Wood chemistry and wood biotechnology*; Walter de Gruyter: 2009.
- [6] Schaechter, M., *Encyclopedia of microbiology*; Academic Press: 2009.
- [7] Ebringerová, A.; Heinze, T. Xylan and xylan derivatives–biopolymers with valuable properties, 1. Naturally occurring xylans structures, isolation procedures and properties. *Macromolecular rapid communications* **2000**, *21*, 542–556.
- [8] Cook, E., *Agriculture, forestry and fishery statistics: 2020 edition*, 2020.
- [9] Industries, T. S. F. The Swedish Forest Industries' statistics on raw materials: 2021, <https://www.forestindustries.se/forest-industry/statistics/raw-materials/>, Accessed: 2023-10-14, 2021.
- [10] Ebringerová, A.; Hromádková, Z.; Heinze, T. Hemicellulose. *Polysaccharides I: Structure, characterization and use* **2005**, 1–67.
- [11] Lantmännen Lantmännen's harvest forecast, Sweden: 5.3 million ton of grain, <https://www.lantmannen.com/about-lantmannen/newsroom/harvest-2022/harvest-forecast-2022/>, Accessed: 2023-10-16, 2022.
- [12] Marcotuli, I.; Hsieh, Y. S.-Y.; Lahnstein, J.; Yap, K.; Burton, R. A.; Blanco, A.; Fincher, G. B.; Gadaleta, A. Structural variation and content of arabinoxylans in endosperm and bran of durum wheat (*Triticum turgidum* L.) *Journal of agricultural and food chemistry* **2016**, *64*, 2883–2892.
- [13] Saulnier, L.; Sado, P.-E.; Branlard, G.; Charmet, G.; Guillon, F. Wheat arabinoxylans: exploiting variation in amount and composition to develop enhanced varieties. *Journal of Cereal Science* **2007**, *46*, 261–281.

- 
- [14] Santibáñez, L.; Henríquez, C.; Corro-Tejeda, R.; Bernal, S.; Armijo, B.; Salazar, O. Xylooligosaccharides from lignocellulosic biomass: A comprehensive review. *Carbohydrate Polymers* **2021**, *251*, 117118.
- [15] Apprich, S.; Tirpanalan, Ö.; Hell, J.; Reisinger, M.; Böhmendorfer, S.; Siebenhandl-Ehn, S.; Novalín, S.; Kneifel, W. Wheat bran-based biorefinery 2: Valorization of products. *LWT-Food Science and Technology* **2014**, *56*, 222–231.
- [16] Brouns, F.; Hemery, Y.; Price, R.; Anson, N. M. Wheat aleurone: separation, composition, health aspects, and potential food use. *Critical reviews in food science and nutrition* **2012**, *52*, 553–568.
- [17] Saake, B.; Kruse, T.; Puls, J. Investigation on molar mass, solubility and enzymatic fragmentation of xylans by multi-detected SEC chromatography. *Bioresource technology* **2001**, *80*, 195–204.
- [18] Bosmans, T. J.; Stépán, A. M.; Toriz, G.; Renneckar, S.; Karabulut, E.; Wagberg, L.; Gatenholm, P. Assembly of debranched xylan from solution and on nanocellulosic surfaces. *Biomacromolecules* **2014**, *15*, 924–930.
- [19] Heikkinen, S. L.; Mikkonen, K. S.; Pirkkalainen, K.; Serimaa, R.; Joly, C.; Tenkanen, M. Specific enzymatic tailoring of wheat arabinoxylan reveals the role of substitution on xylan film properties. *Carbohydrate polymers* **2013**, *92*, 733–740.
- [20] De Man, W. L.; Vaneckhaute, E.; De Brier, N.; Wouters, A. G.; Martens, J. A.; Breynaert, E.; Delcour, J. A. 1H diffusion-ordered nuclear magnetic resonance spectroscopic analysis of water-extractable arabinoxylan in wheat (*Triticum aestivum* L.) flour. *Journal of Agricultural and Food Chemistry* **2021**, *69*, 3912–3922.
- [21] Andrewartha, K. A.; Phillips, D. R.; Stone, B. A. Solution properties of wheat-flour arabinoxylans and enzymically modified arabinoxylans. *Carbohydrate Research* **1979**, *77*, 191–204.
- [22] Yu, L.; Yakubov, G. E.; Gilbert, E. P.; Sewell, K.; van de Meene, A. M.; Stokes, J. R. Multi-scale assembly of hydrogels formed by highly branched arabinoxylans from *Plantago ovata* seed mucilage studied by USANS/SANS and rheology. *Carbohydrate Polymers* **2019**, *207*, 333–342.
- [23] Palasingh, C.; Ström, A.; Amer, H.; Nypelö, T. Oxidized xylan additive for nanocellulose films—A swelling modifier. *International Journal of Biological Macromolecules* **2021**, *180*, 753–759.
- [24] Littunen, K.; Kilpeläinen, P.; Junka, K.; Sipponen, M.; Master, E. R.; Seppälä, J. Effect of xylan structure on reactivity in graft copolymerization and subsequent binding to cellulose. *Biomacromolecules* **2015**, *16*, 1102–1111.

- 
- [25] Borjesson, M.; Westman, G.; Larsson, A.; Strom, A. Thermoplastic and flexible films from arabinoxylan. *ACS Applied Polymer Materials* **2019**, *1*, 1443–1450.
- [26] Farhat, W.; Venditti, R.; Ayoub, A.; Prochazka, F.; Fernández-de Alba, C.; Mignard, N.; Taha, M.; Becquart, F. Towards thermoplastic hemicellulose: Chemistry and characteristics of poly-( $\epsilon$ -caprolactone) grafting onto hemicellulose backbones. *Materials & Design* **2018**, *153*, 298–307.
- [27] Schooneveld-Bergmans, M.; Beldman, G.; Voragen, A. Structural features of (glucurono) arabinoxylans extracted from wheat bran by barium hydroxide. *Journal of Cereal Science* **1999**, *29*, 63–75.
- [28] Köhnke, T.; Pujolras, C.; Roubroeks, J. P.; Gatenholm, P. The effect of barley husk arabinoxylan adsorption on the properties of cellulose fibres. *Cellulose* **2008**, *15*, 537–546.
- [29] Pietiäinen, S.; Moldin, A.; Ström, A.; Malmberg, C.; Langton, M. Effect of physicochemical properties, pre-processing, and extraction on the functionality of wheat bran arabinoxylans in breadmaking—A review. *Food Chemistry* **2022**, *383*, 132584.
- [30] Linder, Å.; Bergman, R.; Bodin, A.; Gatenholm, P. Mechanism of assembly of xylan onto cellulose surfaces. *Langmuir* **2003**, *19*, 5072–5077.
- [31] Gröndahl, M.; Teleman, A.; Gatenholm, P. Effect of acetylation on the material properties of glucuronoxylan from aspen wood. *Carbohydrate Polymers* **2003**, *52*, 359–366.
- [32] Pitkänen, L.; Tuomainen, P.; Virkki, L.; Tenkanen, M. Molecular characterization and solution properties of enzymatically tailored arabinoxylans. *International Journal of Biological Macromolecules* **2011**, *49*, 963–969.
- [33] Yu, L.; Yakubov, G. E.; Martínez-Sanz, M.; Gilbert, E. P.; Stokes, J. R. Rheological and structural properties of complex arabinoxylans from *Plantago ovata* seed mucilage under non-gelled conditions. *Carbohydrate polymers* **2018**, *193*, 179–188.
- [34] Verwimp, T.; Van Craeyveld, V.; Courtin, C. M.; Delcour, J. A. Variability in the structure of rye flour alkali-extractable arabinoxylans. *Journal of agricultural and food chemistry* **2007**, *55*, 1985–1992.
- [35] Simon, J.; Fliri, L.; Drexler, F.; Bacher, M.; Sapkota, J.; Ristolainen, M.; Hummel, M.; Potthast, A.; Rosenau, T. Debugging periodate oxidation of cellulose: Why following the common protocol of quenching excess periodate with glycol is a bad idea. *Carbohydrate Polymers* **2023**, *310*, 120691.

- [36] Buist, G.; Bunton, C.; Miles, J. 149. The mechanism of oxidation of  $\alpha$ -glycols by periodic acid. Part V. Cyclo hexane-1: 2-diols. *Journal of the Chemical Society (Resumed)* **1959**, 743–748.
- [37] Buist, G.; Bunton, C.; Hipperson, W. The mechanism of oxidation of  $\alpha$ -glycols by periodic acid. Part X. The oxidation of pinacol, and a general discussion of the stability of periodate esters and their role in the mechanism of oxidation. *Journal of the Chemical Society B: Physical Organic* **1971**, 2128–2142.
- [38] Amer, H.; Nypelo, T.; Sulaeva, I.; Bacher, M.; Henniges, U.; Potthast, A.; Rosenau, T. Synthesis and characterization of periodate-oxidized polysaccharides: dialdehyde xylan (DAX). *Biomacromolecules* **2016**, *17*, 2972–2980.
- [39] Börjesson, M.; Larsson, A.; Westman, G.; Ström, A. Periodate oxidation of xylan-based hemicelluloses and its effect on their thermal properties. *Carbohydrate polymers* **2018**, *202*, 280–287.
- [40] Kristiansen, K. A.; Potthast, A.; Christensen, B. E. Periodate oxidation of polysaccharides for modification of chemical and physical properties. *Carbohydrate Research* **2010**, *345*, 1264–1271.
- [41] DRYHURST, G. In *Periodate Oxidation of Diol and Other Functional Groups*, DRYHURST, G., Ed.; Pergamon: 1970, pp 24–54.
- [42] Larsson, P. A.; Berglund, L. A.; Wagberg, L. Ductile all-cellulose nanocomposite films fabricated from core-shell structured cellulose nanofibrils. *Biomacromolecules* **2014**, *15*, 2218–2223.
- [43] Vold, I. M. N.; Kristiansen, K. A.; Christensen, B. E. A study of the chain stiffness and extension of alginates, in vitro epimerized alginates, and periodate-oxidized alginates using size-exclusion chromatography combined with light scattering and viscosity detectors. *Biomacromolecules* **2006**, *7*, 2136–2146.
- [44] Smidsrød, O.; Painter, T. Effect of periodate oxidation upon the stiffness of the alginate molecule in solution. *Carbohydrate Research* **1973**, *26*, 125–132.
- [45] Kim, U.-J.; Wada, M.; Kuga, S. Solubilization of dialdehyde cellulose by hot water. *Carbohydrate polymers* **2004**, *56*, 7–10.
- [46] Schönhals, A.; Kremer, F. In *Polymer Science: A Comprehensive Reference*, Matyjaszewski, K., Möller, M., Eds.; Elsevier: Amsterdam, 2012, pp 201–226.
- [47] Härdelin, L.; Ström, A.; Di Maio, E.; Iannace, S.; Larsson, A. Microcellular foaming of arabinoxylan and PEGylated arabinoxylan with supercritical CO<sub>2</sub>. *Carbohydrate polymers* **2018**, *181*, 442–449.



- 
- [48] Börjesson, M.; Larsson, A.; Westman, G.; Ström, A. A process for preparing modified hemicellulose, EP3700941A1 · 2020-09-02, Accessed: 2023-10-14, 2018.
- [49] Pynn, R. Neutron Scattering: A Primer, [https://neutrons.ornl.gov/sites/default/files/intro\\_to\\_neutron\\_scattering.pdf](https://neutrons.ornl.gov/sites/default/files/intro_to_neutron_scattering.pdf), Accessed: 2023-10-14, 1990.
- [50] Wei, Y.; Hore, M. J. Characterizing polymer structure with small-angle neutron scattering: A Tutorial. *Journal of Applied Physics* **2021**, *129*.
- [51] Rongpipi, S.; Ye, D.; Gomez, E. D.; Gomez, E. W. Progress and opportunities in the characterization of cellulose—an important regulator of cell wall growth and mechanics. *Frontiers in Plant Science* **2019**, *9*, 1894.
- [52] Miller, R. L.; Boyer, R. F.; Heijboer, J X-ray scattering from amorphous acrylate and methacrylate polymers: evidence of local order. *Journal of Polymer Science: Polymer Physics Edition* **1984**, *22*, 2021–2041.
- [53] Nieduszynski, I.; Marchessault, R. Structure of  $\beta$ , D (1 $\rightarrow$  4)-xylan hydrate. *Biopolymers: Original Research on Biomolecules* **1972**, *11*, 1335–1344.
- [54] Gabbay, S.; Sundararajan, P.; Marchessault, R. X-Ray and stereochemical studies on xylan diacetate. *Biopolymers: Original Research on Biomolecules* **1972**, *11*, 79–94.
- [55] Marchessault, R.; Settineri, W. Some comments on the crystallography of xylan hydrate. *Journal of Polymer Science Part B: Polymer Letters* **1964**, *2*, 1047–1051.
- [56] Yui, T.; Imada, K.; Shibuya, N.; Ogawa, K. Conformation of an arabinoxylan isolated from the rice endosperm cell wall by X-ray diffraction and a conformational analysis. *Bioscience, biotechnology, and biochemistry* **1995**, *59*, 965–968.
- [57] Lelliott, C; Atkins, E.; Juritz, J.; Stephen, A. Conformation of the gummy polysaccharide from corm sacs of *Watsonia pyramidata*. *Polymer* **1978**, *19*, 363–367.
- [58] Mikkonen, K. S.; Pitkänen, L.; Liljeström, V.; Mabasa Bergström, E.; Serimaa, R.; Salmén, L.; Tenkanen, M. Arabinoxylan structure affects the reinforcement of films by microfibrillated cellulose. *Cellulose* **2012**, *19*, 467–480.
- [59] Beiner, M. Relaxation in poly (alkyl methacrylate) s: crossover region and nanophase separation. *Macromolecular rapid communications* **2001**, *22*, 869–895.
- [60] Beiner, M.; Huth, H. Nanophase separation and hindered glass transition in side-chain polymers. *Nature materials* **2003**, *2*, 595–599.

- [61] Crépy, L.; Miri, V.; Joly, N.; Martin, P.; Lefebvre, J.-M. Effect of side chain length on structure and thermomechanical properties of fully substituted cellulose fatty esters. *Carbohydrate polymers* **2011**, *83*, 1812–1820.
- [62] Liu, L.; Lyu, D.; Xiang, M.; Men, Y. Side chain packing states of chitosan-based supramolecular derivatives containing long alkyl side chains. *Polymer Crystallization* **2020**, *3*, e10110.
- [63] Cousin, F. In *EPJ Web of Conferences*, 2015; Vol. 104, p 01004.
- [64] Kotlarchyk, M.; Chen, S.-H. Analysis of small angle neutron scattering spectra from polydisperse interacting colloids. *The Journal of chemical physics* **1983**, *79*, 2461–2469.
- [65] Petermann, M.; Dianteill, L.; Zeidi, A.; Vaha Ouloassekpa, R.; Budisavljevic, P.; Le Men, C.; Montanier, C.; Roblin, P.; Cabane, B.; Schweins, R., et al. Arabinoxylan in Water through SANS: Single-Chain Conformation, Chain Overlap, and Clustering. *Biomacromolecules* **2023**, *24*, 3619–3628.
- [66] Falcao, A.; Pedersen, J. S.; Mortensen, K Structure of randomly crosslinked poly (dimethylsiloxane) networks produced by electron irradiation. *Macromolecules* **1993**, *26*, 5350–5364.
- [67] Shrestha, U. R.; Smith, S.; Pingali, S. V.; Yang, H.; Zahran, M.; Breunig, L.; Wilson, L. A.; Kowali, M.; Kubicki, J. D.; Cosgrove, D. J., et al. Arabinose substitution effect on xylan rigidity and self-aggregation. *Cellulose* **2019**, *26*, 2267–2278.
- [68] Gunness, P.; Flanagan, B. M.; Mata, J. P.; Gilbert, E. P.; Gidley, M. J. Molecular interactions of a model bile salt and porcine bile with (1, 3: 1, 4)- $\beta$ -glucans and arabinoxylans probed by  $^{13}\text{C}$  NMR and SAXS. *Food chemistry* **2016**, *197*, 676–685.
- [69] Wan, L.; Yuan, Z.; Wu, B.; Jia, H.; Gao, Z.; Cao, F. Dissolution behavior of arabinoxylan from sugarcane bagasse in tetrabutylammonium hydroxide aqueous solution. *Carbohydrate Polymers* **2022**, *282*, 119037.
- [70] Hammouda, B The SANS toolbox. *NIST Center for Neutron Research*, available at <http://tinyurl.com/SANStoolbox> **2008**.
- [71] Nakamura, Y.; Norisuye, T. In *Polymer Science: A Comprehensive Reference*, Matyjaszewski, K., Möller, M., Eds.; Elsevier: Amsterdam, 2012, pp 5–32.
- [72] Palasingh, C.; Nakayama, K.; Abik, F.; Mikkonen, K. S.; Evenäs, L.; Ström, A.; Nypelö, T. Modification of xylan via an oxidation–reduction reaction. *Carbohydrate Polymers* **2022**, *292*, 119660.
- [73] Dyamenahalli, K; Famili, A; Shandas, R In *Shape memory polymers for biomedical applications*; Elsevier: 2015, pp 35–63.

- 
- [74] Swallowe, G. M., *Mechanical Properties and Testing of Polymers: an A–Z reference*; Springer Science & Business Media: 1999; Vol. 3.
- [75] Leyva-Porras, C.; Cruz-Alcantar, P.; Espinosa-Solís, V.; Martínez-Guerra, E.; Piñón-Balderrama, C. I.; Compean Martínez, I.; Saavedra-Leos, M. Z. Application of differential scanning calorimetry (DSC) and modulated differential scanning calorimetry (MDSC) in food and drug industries. *Polymers* **2019**, *12*, 5.
- [76] Muller, F.; Manet, S.; Jean, B.; Chambat, G.; Boue, F.; Heux, L.; Cousin, F. SANS measurements of semiflexible xyloglucan polysaccharide chains in water reveal their self-avoiding statistics. *Biomacromolecules* **2011**, *12*, 3330–3336.
- [77] Muller, F.; Jean, B.; Perrin, P.; Heux, L.; Boué, F.; Cousin, F. Mechanism of associations of neutral semiflexible biopolymers in water: the xyloglucan case reveals inherent links. *Macromolecular Chemistry and Physics* **2013**, *214*, 2312–2323.
- [78] Nylander, F.; Svensson, O.; Josefson, M.; Larsson, A.; Westman, G. New features of arabinoxylan ethers revealed by using multivariate analysis. *Carbohydrate polymers* **2019**, *204*, 255–261.
- [79] Brown, H. Polymer degradation by crazing and its study by small angle scattering techniques. *Materials Science Reports* **1987**, *2*, 317–370.
- [80] Paredes, E.; Fischer, E. W. Röntgenkleinwinkel-untersuchungen zur struktur der crazes (fließzonen) in polycarbonat und polymethylmethacrylat. *Die Makromolekulare Chemie: Macromolecular Chemistry and Physics* **1979**, *180*, 2707–2722.
- [81] Rottler, J.; Robbins, M. O. Growth, microstructure, and failure of crazes in glassy polymers. *Physical Review E* **2003**, *68*, 011801.
- [82] Arbe, A.; Genix, A.-C.; Colmenero, J.; Richter, D.; Fouquet, P. Anomalous relaxation of self-assembled alkyl nanodomains in high-order poly (n-alkyl methacrylates). *Soft Matter* **2008**, *4*, 1792–1795.
- [83] Deralia, P. K.; Sonker, A. K.; Lund, A.; Larsson, A.; Ström, A.; Westman, G. Side chains affect the melt processing and stretchability of arabinoxylan biomass-based thermoplastic films. *Chemosphere* **2022**, *294*, 133618.
- [84] Hiller, S.; Pascui, O.; Budde, H.; Kabisch, O.; Reichert, D.; Beiner, M. Nanophase separation in side chain polymers: new evidence from structure and dynamics. *New Journal of Physics* **2004**, *6*, 10.
- [85] Stepan, A.; Höije, A.; Schols, H.; De Waard, P.; Gatenholm, P. Arabinose content of arabinoxylans contributes to flexibility of acetylated arabinoxylan films. *Journal of Applied Polymer Science* **2012**, *125*, 2348–2355.

